Design and validation of a mathematical model to describe macrophage dynamics in wound healing

A Thesis

Submitted to the Faculty

of

Drexel University

by

Tony Yu

in partial fulfillment of the

requirements for the degree

of

Master's of Science in Biomedical Engineering

August 2014

Acknowledgements

Special thanks to my research advisor and professor, Dr. Kara Spiller, who has given me valuable mentorship, provided exceptional motivation, guided me throughout the duration of my master thesis, and helped me become recipients of the prestigious Whitaker Fellowship and the Outstanding Master Research.

I would like to acknowledge Dr. Wei Liu and the professors at the Shanghai Key Tissue Engineering Laboratory of the Shanghai Jiao Tong University for providing such hospitality during my co-op in their laboratory.

I would also like to thank my committee members, Dr. Margaret Wheatley, Dr. Kambiz Pourrezaei, and Dr. Yinghui Zhong, for providing helpful and insightful critiques on my master's thesis.

I would like to acknowledge and thank my academic advisor, Caryn Glaser, and the biomed faculty whom have given me valuable personal, academic, and professional advices.

I would like to thank all the graduate students in the Biomaterial and Regenerative Medicine Laboratory who have helped me with my research and master's thesis. Specifically, thanks to Sina Nassiri, Val Tutwiler, Pam Graney, Claire Witherel, and Amanda Penetecost

I would also like to thank all the graduate and medical students in the Shanghai Key Tissue Engineering Laboratory of the Shanghai Jiao Tong University. Specifically, Thomas Kwan, Wang Wenbo, Yueqian Zhu, Chen Lulu, and Lian Jie

I would like to acknowledge Dr. Paul Harrington, Laura Knoll, and the CLMP team for their full support during my time at Drexel University

Lastly, I would like to thank a couple of undergraduates for helping me with my experiments, Chau Dang and Dev Patel

Table of Contents

List of Tables ix

List of Figures xi

Abstract xiv

Chapter 1: Introduction 1

1.1 The foreign body response and consequences for implanted biomaterials 2

1.1.1 Diffusion-dependent biomedical devices 4

1.1.2 Transmission of electrical signals 6

1.1.3 Vascularization and integration of biomaterials 7

1.2 Strategies to inhibit the FBR 8

1.2.1 Inhibition of protein adsorption 8

1.2.2 Surface modification with bioactive coatings 9

1.2.3 Surface topography 10

1.3 Macrophage biology 12

1.3.1 Macrophage phenotypes in normal wound healing 12

1.3.2 The role of M1 macrophages in wound healing 13

1.3.3 The role of M2 macrophages in wound healing 15

1.3.4 Role of M1 and M2 macrophages in the FBR to biomaterials 16

1.4 Macrophage polarization in response to biomaterials 20

1.4.1 Decellularized biological scaffolds 20

1.4.2 Porosity of biomaterials 21

1.5 Active control over macrophage phenotype 22

Chapter 2: Experimental design 24

2.1 Specific aim 1: Design and validate a mathematical model to describe macrophage polarization in normal wound healing 25

2.2 Specific aim 2: Design and characterize model biomaterials to assess the foreign body response in vivo. 27

2.3 Specific aim 3: Apply the model to determine if the macrophage dynamics surrounding the implanted biomaterials differs from those in normal wound healing. 28

Chapter 3: Specific Aim 1 29

3.1 Background and derivation 29

3.1.1 Existing mathematical models 29

3.1.2 Biology of mathematical model 30

3.1.3 Criteria for mathematical model 31

3.1.4 Assumptions 32

3.1.5 Mathematical model derivation 32

3.2. Methods 36

3.2.1. *In vitro* experiments for mathematical model 36

3.2.1.a Cell viability of macrophage phenotypes 36

3.2.1.b. Flow cytometry of macrophage phenotypes 37

3.3 Results 37

3.3.1 *In vitro* experiments for mathematical model 37

3.3.1.a Cell viability of macrophage phenotypes 37

3.3.2 Determination of parameter values 41

3.3.3 Results: Model of macrophage profile in normal wound healing 46

Chapter 4: Specific Aim 2 48

4.1. Design criteria 48

4.2 Methods 48

4.2.1. Preparation of glutaraldehyde and glycine 48

4.2.2 Preparation of sodium citrate and sodium phosphate 48

4.2.3. Preparation of crosslinked gelatin hydrogels 49

4.2.4 Hydrogel characterization 49

4.2.4.a Mechanical testing and Young's modulus of hydrogels 49

4.2.4.b Degradation of gelatin hydrogels 50

4.2.4.c Swelling ratio of hydrogels 50

4.2.4.d Crosslinking density of hydrogels 51

4.2.5 Statistical analysis 51

4.3 Results 51

4.3.1 *In vitro* hydrogel characterization 51

Chapter 5: Specific Aim 3 53

5.1. Experimental design 53

5.2 Methods 54

5.2.1 *In vivo* implantation subcutaneously in mice 54

5.2.2 Explanting and paraffin embedding samples and sectioning 55

5.2.3 Histological analyses 56

5.2.3.a Deparaffinization of sectioned samples 56

5.2.3.b H&E staining 56

5.2.3.c Masson's trichrome staining 57

5.2.3.d Immunohistochemistry staining 58

5.2.4 Imaging and quantification 59

5.2.5 Statistical analysis 60

5.3. Results 60

5.3.1 Histological and correlation analyses 60

5.3.1.a H&E staining and quantification 60

5.3.1.b Masson's trichrome stain 65

5.3.1.c Macrophage phenotyping by immunohistochemistry 71

5.3.2 Correlation Analyses 80

Chapter 6: Discussion 82

Chapter 7: Conclusions 89

Chapter 8: List of References 90

List of Tables

Table 1: The raw data of the cell viability of the concentration (cells/mL) of each macrophage population [76] 38

Table 2: The raw data of flow cytometry as reported as the percentage of positive cells that express M1 or M2 characteristics for each macrophage phenotype [76] 40

Table 3: The survival expression of each of the macrophage populations 44

Table 4: The rate constants that were calculated by the survival expression term 45

Table 5: The polarization and transition rates of each of the macrophage population 45

Table 6: List of all the parameters with its respective values of the mathematical model 46

Table 7: The MATLAB quantification of the fibrous capsule from the H&E images 64

Table 8: Masson's trichrome quantification of the fibrous capsule thickness on both sides of the hydrogel (units are in um)..... 70

Table 9: Quantification of the intensities of the three surface markers 79

Table 10: M1:M2 ratio to indicate the macrophage phenotype at each time point 80

Table 11: Correlation coefficients of the M1:M2 ratio and iNOS, Arg1, and CD163 to the fibrous capsule thickness 82

List of Figures

Figure 1: Progression of the foreign body response. Upon implantation of the biomaterial (A) proteins from the blood and tissue nonspecifically adsorb to the biomaterial surface (B), and the coagulation cascade is initiated (C). Neutrophils and monocytes are recruited during the acute inflammatory phase (D). Monocytes differentiate into macrophages which attempt to degrade the biomaterial. If the macrophages cannot degrade the material they fuse into foreign body giant cells, the hallmark of chronic inflammation (E). These multinucleated cells stimulate formation of granulation tissue, which eventually becomes a dense fibrous collagen capsule that isolates the biomaterial from the rest of the body (F)..... 2

Figure 2: Biomaterials particularly sensitive to the foreign body response. A. Glial scarring in around implanted microelectrodes can block the conductance of neuronal activity. B. Vascularization, critical for the functionality of some implants, is blocked by fibrous encapsulation. C. The fibrous capsule acts as a diffusion barrier, decreasing the performance of diffusion-dependent biomaterials such as drug delivery devices and glucose sensors..... 4

Figure 3: Macrophages in normal wound healing. A. In normal wound healing, macrophages initially express a pro-inflammatory response but as time progress they transition to a pro-healing response. B. Macrophages can be polarized into a spectrum of phenotypes that range from a pro-inflammatory to a pro-healing response. Those discussed here include: M1 macrophages which are induced through by TNF-α and LPS, M2a macrophages which are stimulated by IL-4, and M2c macrophages which are activated by IL-10. 12

Figure 4: A schematic of the experimental design. A. The development of a mathematical model that models macrophages in normal wounding based on in vitro experiments. B. In vitro characterization of crosslinked gelatin hydrogels, which were implanted in mice at different time points to evaluate the macrophage phenotypes via histology..... 25

Figure 5: Cell viability calculated by the fold change over day 0 of each macrophage population [76]..... 39

Figure 6: The macrophage expression of M1 and M2 characteristics in flow cytometry [76]..... 41

Figure 7: The output of the model representing M0, M1, and M2 macrophage profile in normal wound healing..... 47

Figure 8: The crosslinked hydrogels characterized by the hydrogel properties. A. The crosslinking density is significant from each hydrogel. B. The stiffness of each hydrogel is significantly difference. C. The 0.3% hydrogel was significantly difference from the other two hydrogels. D. The degradation of each hydrogels were significantly different from day 7 to day 13. * indicates statistical significance ($p<0.05$) between the indicated groups. ** denotes $p<0.01$, *** denotes $p<0.005$, **** denotes $p<0.001$ 52

Figure 9: A schematic of the locations in which the crosslinked hydrogels were implanted subcutaneously per mice. A hydrogel with different crosslinking concentration was implanted for each location..... 55

Figure 10: A MATLAB code that quantifies the fibrous capsule via image processing.. 61

Figure 11: The thickness of the fibrous capsule was measured in ImageJ to verify the MATLAB quantification. 62

Figure 12: A labeled H&E image to illustrate the infiltration of cell surrounding the hydrogel. 63

Figure 13: H&E images showing the difference in fibrous capsule of the 3 crosslinked hydrogels at the 3 time point..... 64

Figure 14: Graphical representation of the thickness of the fibrous capsule quantified using the MATLAB code from H&E images. * denotes $p<0.05$, *** denotes $p<0.005$.. 65

Figure 15: Labeled Masson's trichrome image to illustrate the collagen and infiltration of cells around the hydrogels 66

Figure 16: A 4x magnification of the Masson's trichrome stain of a 3 day 0.1% hydrogel zoomed in to a 20x magnification at both sides of the hydrogel 67

Figure 17: A 4x magnification of the Masson's trichrome stain of a 10 day 0.1% hydrogel zoomed in to a 20x magnification at both sides of the hydrogel 68

Figure 18: A 4x magnification of the Masson's trichrome stain of a 3 week 0.3% hydrogel zoomed in to a 20x magnification at both sides of the hydrogel 68

Figure 19: Masson's trichrome images at 10x magnification showing the difference in fibrous capsule of the 3 crosslinked hydrogels at the 3 time points. 69

Figure 20: The comparison between the fibrous capsule thickness quantified from H&E and the fibrous capsule thickness quantified from Masson's trichrome. * denotes $p<0.05$, *** denotes $p<0.005$. 71

Figure 21: The negative and positive controls of an IHC stain. 72

Figure 22: The intensity of the IHC staining was quantified within the yellow rectangular boxes. 73

Figure 23: iNOS staining quantification at 20x magnification of the 3 crosslinked hydrogels at the 3 time points. 74

Figure 24: Arg1 staining quantification at 20x magnification of the 3 crosslinked hydrogels at the 3 time points. 76

Figure 25: CD163 staining quantification at 20x magnification of the 3 crosslinked hydrogels at the 3 time points. 77

Figure 26: The quantification of the fibrous capsule thickness and the macrophage phenotype. A. Quantification of the thickness of the fibrous capsule. B. Quantification of iNOS staining. C. Quantification of Arg1 staining. D. Quantification of CD163 staining. * denotes $p<0.05$, *** denotes $p<0.005$..... 78

Figure 27: The correlation analyses to the fibrous capsule thickness. A. The correlation between the M1:M2 ratio and the fibrous capsule. B. The correlation between the iNOS intensity and the fibrous capsule. C. The correlation between the Arg1 intensity and the fibrous capsule. D. The correlation between the CD163 intensity and the fibrous capsule. 81

Figure 28: A comparison of a chronic wound via deletion of the M1-to-M2 term to the normal wound healing model..... 85

Abstract

Design and validation of a mathematical model to describe macrophage dynamics in wound healing
Tony Yu
Kara Spiller, PhD.

Macrophages have been shown to play an essential role in regulating the foreign body response, and understanding and modulating the macrophage dynamics in wound healing could potentially help overcome their ability to impair biomaterial performance. However, *in vivo* animal studies are often utilized to study the macrophage dynamics, which are costly and time consuming. Although there have been previous models that describe the macrophage behavior and the foreign body response, many of the parameters of these models were not based on experiments and are not physiologically relevant to macrophage biology. Therefore, there is a need to develop a model that can help predict the *in vivo* foreign body response in wound healing based on *in vitro* and/or *in vivo* experiments. In this study, a mathematical model was developed to describe the macrophage dynamics (M0, M1, and M2) in normal wound healing based on cell viability and flow cytometry experiments of unactivated and polarized macrophages cultured *in vitro*. The ordinary differential equations that describe the macrophage populations take into consideration the polarization, transition, and proliferation of surviving macrophages within each population, resulting in an accurate description of macrophage biology.

This mathematical model was then applied to describe macrophage dyanmics an *in vivo* study of the macrophage response to implanted biomaterials, which have often been described as chronic wounds. Gelatin hydrogels, crosslinked to different extents, were used as model biomaterials. The hydrogels were characterized for properties including mechanical stiffness, degradation, swelling, and crosslinking density, and were implanted subcutaneously in C57BL/6 mice for 3 day, 10 days, and 3 weeks. H&E, Masson's trichrome, and immunohistochemistry were performed on these samples to quantify the thickness of the fibrous capsule and the relative proportions of different macrophage populations.

The mathematical model was able to describe the macrophage profiles that were consistent with normal wound healing. In this model, an initial inflammatory response was observed, followed by an accumulation of M2 macrophages over time. The implanted hydrogels imposed a chronic inflammation throughout the study with a constant infiltration of M1 macrophages. The M2 macrophages behaved in a similar manner to that of normal wound healing, with a slow and gradual accumulation of M2 macrophages over time. The M1:M2 ratio indicated a dominant M1 phenotype at the early time point. At the later time point, a ratio of 1 indicated an even distribution of M1 and M2 macrophages. Correlation analyses showed that the M2 macrophages were strongly correlated with fibrous capsule thickness. Thus, the mathematical model developed here can be used to increase our understanding of macrophage dynamics in wound healing and response to biomaterials.

Chapter 1: Introduction

Biomaterials are part of the solution to many unmet clinical needs, from implantable sensors to drug delivery devices and engineered tissues. However, biomaterials face an inflammatory environment upon implantation, which represents a potential obstacle to their success [1]. In this chapter, we review the consequences of the foreign body response (FBR) for biomaterial function, and strategies that have been used to inhibit the FBR. We focus on the role of the macrophage, the cell at the center of the inflammatory response, as the major regulator of the FBR, and discuss implications of changing macrophage behavior on biomaterial acceptance or rejection. Finally, we discuss recent discoveries in the role of macrophage phenotype, ranging from pro-inflammatory (M1) to anti-inflammatory (M2), and the role it plays in wound healing and biomaterial vascularization and integration. We conclude with a discussion of biomaterial design strategies that have been suggested to positively interact with and potentially control macrophages in order to improve interactions between biomaterials and the inflammatory response.

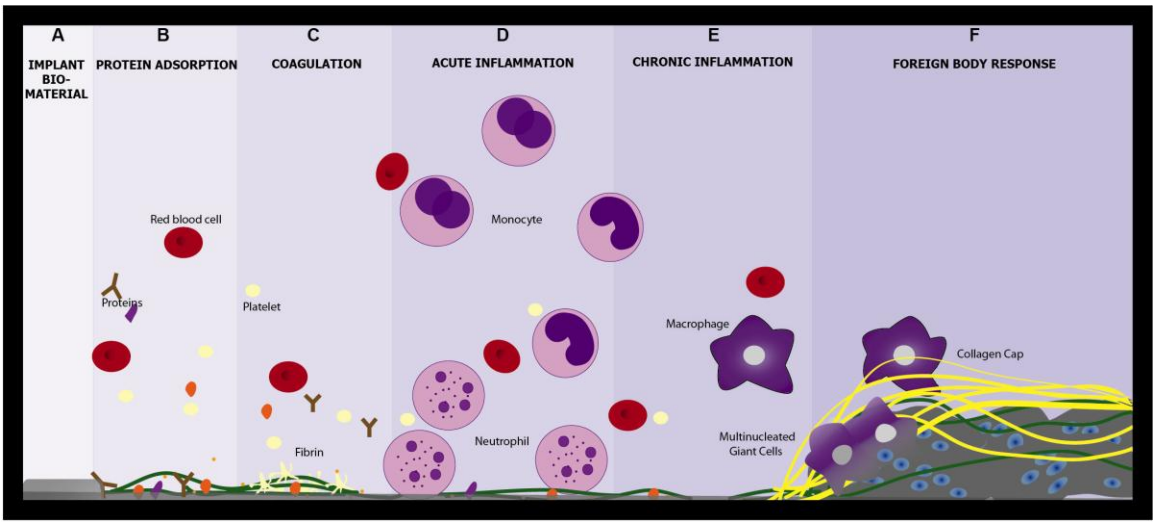

Figure 1: Progression of the foreign body response. Upon implantation of the biomaterial (A) proteins from the blood and tissue nonspecifically adsorb to the biomaterial surface (B), and the coagulation cascade is initiated (C). Neutrophils and monocytes are recruited during the acute inflammatory phase (D). Monocytes differentiate into macrophages which attempt to degrade the biomaterial. If the macrophages cannot degrade the material they fuse into foreign body giant cells, the hallmark of chronic inflammation (E). These multinucleated cells stimulate formation of granulation tissue, which eventually becomes a dense fibrous collagen capsule that isolates the biomaterial from the rest of the body (F).

1.1 The foreign body response and consequences for implanted biomaterials

Upon implantation (Fig. 1a), the body mounts the FBR against the biomaterial, beginning with protein adsorption to the biomaterial surface (Fig. 1b) [2]. This creates a thrombogenic surface and results in the activation and aggregation of a platelet-fibrin meshwork (Fig. 1c) [3]. The resulting pro-coagulant surface results in the infiltration of inflammatory cells. Neutrophils are the first inflammatory cells to arrive at the biomaterial surface [4]. When these cells are unable to phagocytose the foreign body, cytokines are released, which result in the differentiation of macrophages from monocytes [5]. Of the recruited immune cells, macrophages are the main cell type that regulates the FBR. At this point in normal wound healing, the acute inflammation phase

(Fig. 1d) would ebb and proliferation of fibroblasts and eventually remodeling of the wound would occur [4]. However, in response to an implanted biomaterial the macrophages continue to attempt to remove the foreign body via phagocytosis and secrete enzymes and reactive species that aggravate the inflammatory state [6]. As a result, the progression through normal wound healing is disturbed and a chronic inflammation phase ensues (Fig. 1e) [7]. If the biomaterial cannot be degraded, the macrophages fuse together to form multinucleated foreign body giant cells (FBGC) that surround the biomaterial [8]. FBGCs and recruited fibroblasts deposit collagen layers around the biomaterial to form granulation tissues [9]. Over time, the granulation tissue becomes a dense collagen capsule, the hallmark of the FBR (Fig. 1f) [9]. Isolation of the biomaterial within this capsule as well as the secretion of damaging enzymes jeopardizes the functioning of the biomaterial. Some biomaterial applications that are particularly sensitive to the FBR include drug delivery devices, sensory devices, electrical devices, and tissue engineered constructs.

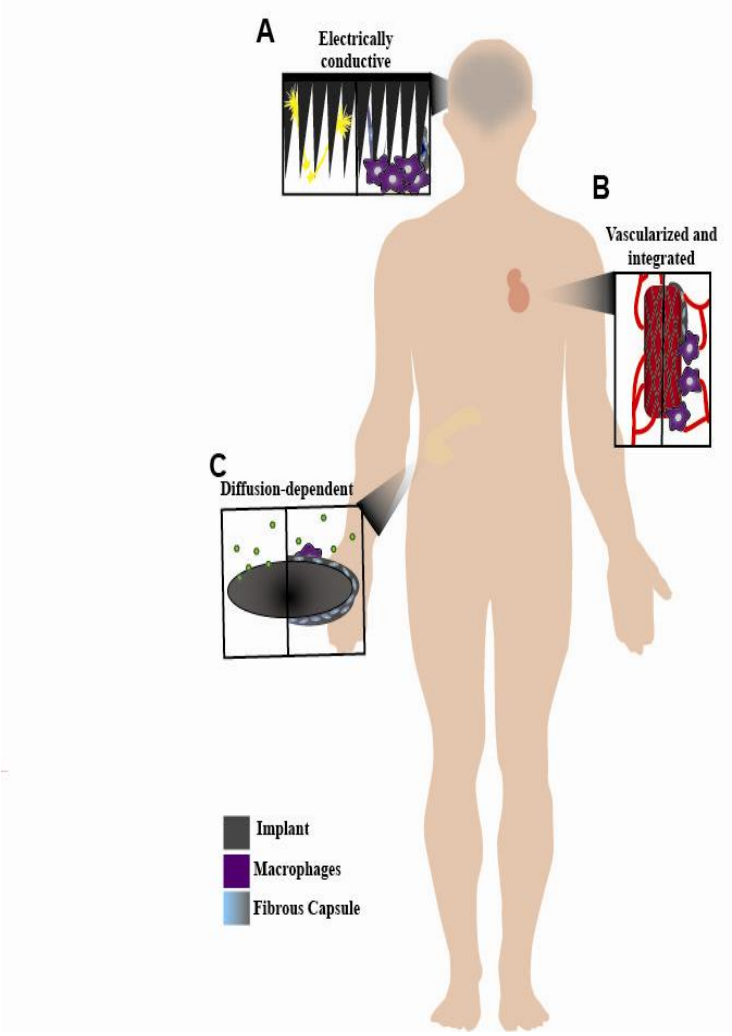

Figure 2: Biomaterials particularly sensitive to the foreign body response. A. Glial scarring in around implanted microelectrodes can block the conductance of neuronal activity. B. Vascularization, critical for the functionality of some implants, is blocked by fibrous encapsulation. C. The fibrous capsule acts as a diffusion barrier, decreasing the performance of diffusion-dependent biomaterials such as drug delivery devices and glucose sensors.

1.1.1 Diffusion-dependent biomedical devices

Biomaterials that depend on diffusion of molecules for their function include drug delivery systems, which are used to locally delivery drugs or growth factors to a particular area of the body, and sensors that measure the level of a molecule in the blood or tissue, including glucose sensors (Figure 2a). Fibrous encapsulation can hinder

diffusion, thus adversely affecting the function of the biomaterial [10]. For example, Anderson et al. investigated the drug release of gentamicin, an antibiotic, from silicone rubber rods [11]. Liquid-scintillation counting was performed to determine the release of radiolabeled gentamicin as well as the concentration in tissues adjacent to the implant. The rods were coated with a layer of silicon rubber to reduce the initial burst release and to prolong the drug release over time. The silicon rod drug release system with different gentamicin loading dosages (20, 35, and 40 wt%) were implanted intramuscularly at the thigh muscles in dogs for 1 day, 1, 2, and 4 weeks. A fibrous capsule of about 5 um and 11-15 um thick was observed at 2 and 4 weeks post-implantation, respectively. Along with the observation of connective tissues forming around the implants, a reduction of the drug release rate was observed over the 4 week period. In addition, the difference in the gentamicin tissue level and serum levels over the first 3 weeks indicated that there was another factor with a different diffusion coefficient that may be responsible for the reduction in the drug release rate. As a result, it was suggested that formation of the fibrous capsule inhibited the release of gentamicin [11].

One of the most common medical devices to monitor diabetes is the continuous glucose monitor (CGM), which monitors the blood glucose level via diffusion of blood glucose to the glucose sensor [12]. The FBR can hinder this function, as is demonstrated by a study in which macrophage depletion with diphtheria toxin driven by the CD11b promoter improved sensor performance [13]. While the creation of a diffusion barrier by the fibrous capsule likely inhibits sensor performance, it may also be a result of macrophage metabolic activity [14]. Klueh et al. injected macrophages at the implantation site of glucose sensors in mice [12]. The macrophages surrounded the

sensors and sensor output quickly diminished, an effect that was not observed with injected lymphocytes. Interestingly, when serum glucose levels were artificially elevated, they were detected by the sensors, suggesting that their function was not permanently impaired by the presence of the macrophages. Moreover, companion *in vitro* studies showed that the presence of macrophages without the fibrous capsule or other biofouling effects also hindered sensor performance. The authors concluded that metabolism of glucose by macrophages also contribute to decreased sensor performance [12].

1.1.2 Transmission of electrical signals

Some medical devices require the conductance of electrical signals in order to monitor or pace the electrical activity of the brain, heart, or other muscles in the body, but the transmission of these signals can be inhibited by the presence of a fibrous capsule or a glial scar, as is the case in the central nervous system (Figure 2b) [15]. A common electrical recording device is the silicon microelectrode array, a technology that measures the neuronal activity in the brain that is often used to monitor the activity of neurons and/or to investigate the correlation between the brain activity and behavior. However, one of the main limitations of this technology is inconsistency of performance in long term applications. In a study by Biran et al. [16], the silicon microelectrode array was implanted into the brains of rats for 2 and 4 weeks to determine the mechanism of failures of the microelectrode arrays. Stab wounds were also created with the same microelectrodes as controls in order to distinguish whether it was the initial penetrating trauma or the FBR to the chronically implanted microelectrodes that caused device

failure. After 2 and 4 weeks post-implantation, immunohistochemical analysis of the brain tissue indicated multilayered and dense regions of ED1-positive cells, a pan-macrophage marker in rats, along the implant-brain tissue interface in both the stab wounds and implanted microelectrodes. However, there were more ED1-positive cells surrounding the implanted microelectrodes compared to the stab wound. The intensity of glial fibrillary acidic proteins (GFAP) expression by reactive astrocytes was also significantly higher surrounding implanted microelectrodes compared to the control stab wounds. There was a significant amount of neuronal loss 2 weeks post-implantation in the nearby tissue of the implanted microelectrodes compared to the stab wound. Explants were rinsed with PBS and cultured in media for 24 hours to assess cytokine secretion by adherent macrophages, which showed secretions of the inflammatory cytokines tumor necrosis factor-alpha (TNF- α) and monocyte chemotactic protein (MCP-1). Thus, the presence of the foreign body increased inflammation, leading to neuronal loss and device failure [16].

1.1.3 Vascularization and integration of biomaterials

Tissue engineering holds tremendous potential to replace damaged tissues and organs. The success of most tissue engineered constructs requires recruitment of endothelial cells and formation of new blood vessels to provide nutrient and oxygen transport for implanted cells [17, 18]. However, the FBR and the fibrous capsule prevent direct contact between the biomaterial and the surrounding tissue, so that vascularization and integration are essentially blocked (Figure 2c). Shin et al. showed that fibrous encapsulation of hydrogels based on oligo(poly(ethylene glyocol) fumarate) effectively

prevented bone formation and vascularization in a rabbit bone defect model [19]. More recently, several studies have confirmed inverse correlation between fibrous capsule thickness and blood vessel ingrowth [5, 20].

1.2 Strategies to inhibit the FBR

Clearly, the FBR and the formation of the fibrous capsule can drastically inhibit the function of biomaterials. Thus, researchers have turned to the development of strategies to inhibit the FBR. Because the FBR begins with protein adsorption and inflammatory cell interactions at the biomaterial surface, most strategies are based on modifications of the biomaterial surface [21, 22]. The main strategies include inhibition of protein adsorption, the use of bioactive coatings, and modifications to surface topography.

1.2.1 Inhibition of protein adsorption

Because the FBR begins with protein adsorption, inhibition of protein adsorption has been extensively researched as a tool to inhibit the FBR [23]. PEGylation, hydrogel coatings, plasma treatment, and other methods have shown substantially decreased protein adsorption *in vitro* with reduced fibrous capsule formation *in vivo* [24]. Ultimately, however, the sensors fail because blood proteins can still adsorb to a certain extent [14]. Recently, ultra-low fouling biomaterials have been prepared from zwitterionic materials [21]. Zwitterionic materials have both a positive and negative charge that are not dissociated in an aqueous environment. This property attracts water molecules via charge-dipole interactions resulting in extremely hydrophilic properties

[25]. Thus, adsorption of relatively hydrophobic proteins is drastically reduced. The zwitterion carboxybetaine was shown to adsorb <0.3 ng/cm^2 proteins from 100% blood serum, much lower than the 5 ng/cm^2 of absorbed fibrinogen that is required to initiate platelet adhesion [22]. When zwitterionic hydrogels based on poly(carboxybetaine methacrylate) (PCBMA) were implanted subcutaneously in mice for 3 months, the number of pro-inflammatory macrophages was reduced compared to control hydrogels prepared from poly(2-hydroxyethyl methacrylate) (PHEMA), and the presence of a fibrous capsule was not observed [21].

Thus, inhibition of protein adsorption is an effective way to mitigate the FBR. However, without protein adhesion, cells from the body also cannot infiltrate the material, so these biomaterials may not be appropriate for applications that require integration with the body, such as in tissue engineering. Nonetheless, they may be extremely useful for applications in which the biomaterials are not intended to integrate with body, such as catheters.

1.2.2 Surface modification with bioactive coatings

For biomaterials that are intended to integrate with the body, another strategy to mitigate the FBR and the formation of the fibrous capsule is to make the biomaterial appear less foreign to immune cells, such as by coating with extracellular matrix (ECM)-derived molecules [26]. The ECM is mainly composed of collagen type I and glycosaminoglycans (GAG) such as hyaluronan (HA), chondroitin sulfate, and dermatan sulfate. Coating titanium rods with collagen chondroitin sulfate has been shown to inhibit

fibrous encapsulation and to promote new bone formation in rat tibial defects [27]. Similarly, drug delivery strategies that actively increase integration with the body show decreased fibrous capsule formation. For example, controlled release of VEGF and nitric oxide (NO) from sensors has been shown to increase vascularization and decrease fibrous capsule formation [28, 29]. Controlled release of anti-inflammatory drugs such as dexamethasone has also been shown to reduce the FBR to sensors [30].

1.2.3 Surface topography

Modifications to the surface topography of biomaterials have also been shown to affect the FBR [31]. The addition of porous poly(lactic acid) (PLA) coatings to glucose sensors decreased fibrous capsule thickness and increased vascularity following murine implantation [32]. Cao et al. investigated the orientation of the topography of electrospun nanofibrous poly(caprolactone) (PCL) scaffolds and reported the effect on the FBR [31]. The PCL was deposited in three distinct manners: aligned fibers, randomly oriented fibers, and a thin film; the scaffolds were then compared to an RGD-coated glass slide as a control. IL-4 was added to human monocytes *in vitro* at days 3 and 7 in order to induce the formation of FBGC, mimicking the FBR *in vivo*. At day 10, the random fiber scaffolds resulted in the highest levels of cell attachment compared to the other scaffolds. In general, the cell density of all surfaces decreased over time as the macrophages fused into FBGC in the presences of IL-4. When the PCL scaffolds were implanted in Sprague-Dawley rats for 1, 2, and 4 weeks, the random fiber scaffold elicited a more severe FBR compared to the other scaffolds, while the aligned fiber scaffold resulted in the thinnest

fibrous capsule [31]. Thus, biomaterial topography affects the FBR, and this behavior can be studied using *in vitro* models of macrophage-biomaterial interactions.

This relationship between *in vitro* and *in vivo* results was not supported in another study of the effects of biomaterial topography on the FBR. Expanded polytetrafluoroethylene (ePTFE) membranes with pore sizes of 0.2, 1, and 3 um were seeded with primary human monocytes *in vitro* and compared to tissue culture polystyrene as a control [33]. Membranes with 3um pore size elicited a significant increase in the secretion of the inflammatory cytokine interleukin-1-beta (IL1-β) compared to the other pore sizes. The ePFTE biomaterials were also implanted subcutaneously in mice for 4 weeks to evaluate the formation of the fibrous capsule. Interestingly, despite showing more inflammatory activity *in vitro*, ePTFE membranes with 3um pores resulted in a significantly thinner fibrous capsule than the non-porous ePTFE [33]. Although these findings did show that biomaterial topography affects the FBR, they also highlight the complexity of the relationship between inflammatory cell-biomaterial interactions and the FBR.

While the studies of the effects of biomaterial surface topography on the FBR have been largely empirical, they do suggest that modulation of topography may be a potential tool for mitigating the FBR. More systematic analyses are required to determine the mechanism of topographical effects on macrophage behavior and the FBR.

1.3 Macrophage biology

It has been shown through many studies that macrophages play a crucial role in regulating the FBR [5]. A better understanding of macrophage dynamics may be the key to overcoming their ability to impair biomaterial performance. To understand the behavior of macrophages in response to biomaterials, it is helpful to consider biomaterial implantation as a chronic wound. Then, the behavior of macrophages can be assessed in comparison to normal wound healing in order to discover the mechanisms of impaired healing.

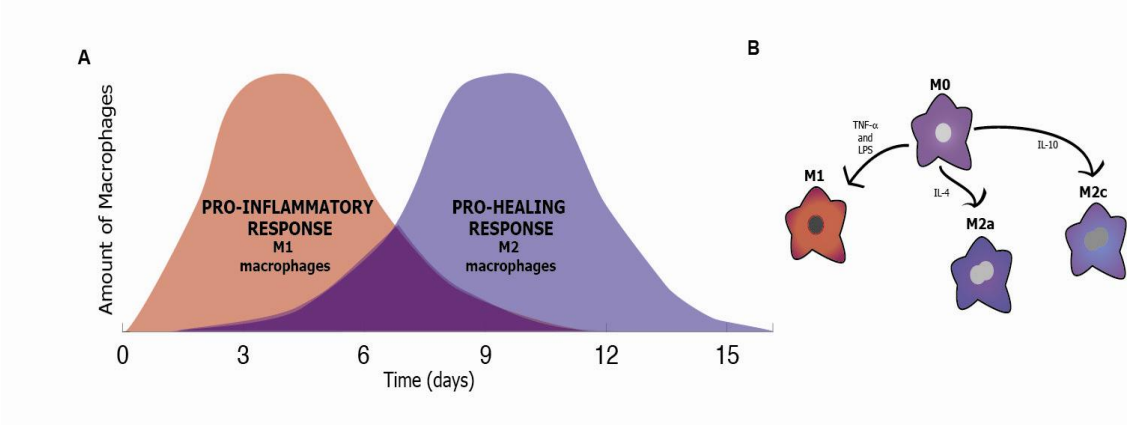

Figure 3: Macrophages in normal wound healing. A. In normal wound healing, macrophages initially express a pro-inflammatory response but as time progress they transition to a pro-healing response. B. Macrophages can be polarized into a spectrum of phenotypes that range from a pro-inflammatory to a pro-healing response. Those discussed here include: M1 macrophages which are induced through by TNF-α and LPS, M2a macrophages which are stimulated by IL-4, and M2c macrophages which are activated by IL-10.

1.3.1 Macrophage phenotypes in normal wound healing

Normal wound healing in response to an injury generally consists of four distinct stages: hemostasis, the inflammatory stage, the proliferation stage, and the remodeling

stage [4, 34, 35]. Macrophages can be polarized into a spectrum of phenotypes ranging from pro-inflammatory to anti-inflammatory and pro-healing depending on the environmental stimulus [36]. Pro-inflammatory macrophages are often referred to as "classically activated", or M1, while the anti-inflammatory macrophages are referred to as "alternatively activated", or M2 phenotype, following the T helper cell nomenclature of Th1 and Th2 [36]. At early stages of normal wound healing, M1 macrophages infiltrate the wound to promote inflammation and to stimulate the wound healing process (Figure 3). M2 macrophages begin to accumulate around day 3 or 4 post-injury, while the level of M1 macrophages decreases [36]. M2 macrophages may accumulate via the direct transition of M1 to M2, the polarization of newly arriving macrophages to M2, and proliferation of other M2 macrophages [37]. The accumulated macrophages eventually emigrate to the draining lymph nodes returning back to the pre-injury state of resident macrophages after the wound is completely remodeled and healed [38].

Macrophages have been widely recognized as major regulators of wound healing and tissue regeneration over the last few decades. However, much of macrophage biology is still not well understood. Although the classification of the different macrophage phenotypes is widely accepted, a consensus has not yet been reached as to the overall effects and consequences of the diverse macrophages phenotypes on wound healing.

1.3.2 The role of M1 macrophages in wound healing

Macrophages are polarized to the M1 phenotype by proinflammatory stimuli and cytokines such as bacterial lipopolysaccharide (LPS), tumor necrosis factor-alpha (TNF-

α), and interferon-gamma (IFN-γ) (Figure 3b) [5]. M1 macrophages attempt to phagocytose any bacteria, cellular debris, and foreign invaders. However, controversies surround the role of M1 macrophages in wound healing. On the one hand, chronic inflammation, characterized by persistent numbers of M1 macrophages, is known to impair wound healing. For example, Kigerl et al. studied the effect of macrophage activation on central nervous system injury of C57BL/6 mice [39]. Moderate midthoracic spinal cord injury (SCI) was inflicted on the mice, while the sham mice receive a laminectomy without SCI. The tissues samples were collected at day 1, 3, 7, 14, and 28 post-SCI for immunohistochemical analysis. M1 macrophages were predominant at the sites of SCI as indicated by CD86 staining. The RNA from each of the wound sites at each time point was extracted for gene expression and showed that the genes associated with the M2 macrophages returned to pre-injury level at day 7 post-SCI, while genes associated with the M1 macrophages were maintained for 1 month post-SCI. These results suggest that the M1 macrophages were responsible for the defective wound healing over time. Furthermore, macrophage-conditioned media (MCM) was also collected from the supernatant of polarized macrophages to determine the effect of M1 and M2 MCM on cortical neurons *in vitro*. The M1 - but not the M2 - MCM was neurotoxic to cortical neurons [39]. Consequently, this study suggests that the M1 macrophages are detrimental to healing.

On the other hand, M1 macrophages have also been shown to be beneficial for wound healing [40]. M1 macrophages are highly angiogenic, stimulating endothelial cell sprout formation *in vitro* and *in vivo* in part by secretion of vascular endothelial-derived growth factor (VEGF) [5, 41]. When M1 macrophages were depleted in a mouse model

of skeletal muscle injury via CD11b-diptheria toxin, muscle regeneration was completely prevented [42]. In contrast, when M2 macrophages were depleted, muscle regeneration was still possible, but it was significantly impaired. However, persistent numbers of M1 macrophages mark chronic inflammation and impaired healing, highlighting the importance of the correct M1-to-M2 sequence in tissue repair.

1.3.3 The role of M2 macrophages in wound healing

M2 macrophages are generally associated with healing and tissue remodeling of the wound and are the dominant phenotype in the proliferation and remodeling stages of wound healing [43]. The M2 macrophages are usually responsible for the formation of connective tissue [44]. However, the granulation tissue may eventually lead to the formation of scar tissue or a fibrous capsule. For this reason, it is believed that the M2 macrophages contribute to the fibrous capsule formation and the FBR [4].

The M2 macrophage phenotype can be further classified into three-subpopulations: M2a, M2b, and M2c [5, 45]. Macrophages are polarized to the M2a and M2c phenotype by environmental stimulation of IL-4 and IL-10, respectively (Figure 3b) [5, 45]. The M2b phenotype is polarized by toll-like receptors (TLC) or other immune complexes [45]. Although the M2b is categorized within the M2 phenotype, the M2b macrophages are activated by an inflammatory environmental stimulus more similar to that of the M1 macrophages [46]. Their role in wound healing is not known. The traditional alternatively activated M2 macrophages are now referred to as the M2a

phenotype, which promotes the production of extracellular matrix (ECM) and collagen, a necessary part of healing [5, 46].

Preliminary studies have attempted to explain the functioning of M1, M2a, and M2c subpopulations in wound healing and vascularization [5], however there is still a great need for further research in this area. M1 macrophages secrete VEGF to initiate angiogenesis. M2a macrophages secrete PDGF, a chemoattractant that stabilizes growing blood vessels and promotes anastomosis of new blood vessels into networks [5]. M2c macrophages secrete high levels of matrix metalloprotease 9 (MMP-9), a protease that is involved in the breakdown and remodeling of the ECM and vasculature [5]. M2c macrophages also express high levels of CD163, which has been shown to be associated with tissue repair and remodeling of the wound and promoting cell proliferation in mice [45]. Thus, it appears that M1, M2a, and M2c macrophages appear sequentially in normal wound healing, but more studies are required that distinguish between M2a and M2c macrophages in order to confirm this hypothesis.

1.3.4 Role of M1 and M2 macrophages in the FBR to biomaterials

Surprisingly, it is still not clear which macrophage phenotype is responsible for the formation of the fibrous capsule. M1 macrophages are widely believed to be the cause of the fibrous capsule as the inflammatory response up-regulates the FBR, thereby increasing the thickness of the fibrous capsule [47]. However, IL-4, a cytokine that induces the activation to the M2a phenotype, has been shown to promote the formation of FBGC, which ultimately causes the formation of the fibrous capsule [5, 48].

To investigate the association of macrophage phenotype and tissue remodeling of biological scaffolds in the FBR, Badylak et al. implanted porcine small intestine submucosa (SIS), carbodiimide crosslinked porcine derived SIS (CDI-SIS), and autologous tissue graft as a control subcutaneously in Sprague-Dawley rats for 1, 2, 4, and 16 weeks [49]. Immunostaining of CCR7 and CD163, representing M1 and M2 markers respectively, showed an infiltration of M2 macrophages in the SIS scaffolds at all time points, along with an organized layer of connective tissue at the 16 week time point, which suggests constructive remodeling. The CDI-SIS scaffolds were initially infiltrated with equal amounts of M1 and M2 macrophages at 2 weeks post-implantation, but were eventually dominated by the M1 macrophages at 4 weeks post-implantation leading to the formation of FBGC and fibrosis at 16 weeks post-implantation. The autologous graft scaffold showed a high level of M2 macrophages at the 1 and 2 week time points, but over time, an even distribution of M1 and M2 macrophages was observed. At the 16 week post-implantation, less organized collagenous connective tissue was also observed. The authors concluded that biomaterials that promote the M2 phenotype are associated with constructive tissue remodeling compared to those that promote the M1 phenotype [49]. This study was one of the first to suggest macrophage phenotype as a predictor of the success or failure of biomaterials.

Brown et al. evaluated the effects of 14 FDA-approved biological scaffolds on macrophage phenotype and the FBR in rats [50]. All scaffolds were composed of naturally occurring material but differed in the source and species of the tissue. The 14 scaffolds included AlloMax, AlloDerm, Avaulta Plus, CollaMend, Flex HD, InteXen LP, MatriStem, PelviSoft, Strattice Firm, Strattice Pliable, Sugisis, SurgiMend, Veritas, and

Xenform. Immunohistochemical analysis of CD68, CCR7, and CD206 was performed on the samples after 14 and 35 days of implantation to quantify the relative proportions of M1 and M2 macrophages at each time point. In general, a higher M2 to M1 ratio was associated with more constructive remodeling [50].

Goreish et al. evaluated the effects of phosphorylcholine (PC) coated biomaterials on the FBR and fibrous capsule formation via intramuscular implantation in rabbits for 4 and 13 weeks, and found that there were less M1 macrophages and a reduced fibrous capsule on the PC-coated biomaterial compared to the control of high-density polyethylene, but were not significantly different at 4 days post-implantation [51]. At 13 weeks post-implantation, little to no M1 macrophages were found at the implantation site for both control and PC-coated biomaterials. The fibrous capsule thickness of the PC-coated biomaterial was reduced to no capsule or partial encapsulation at the 13 week time point, while the fibrous capsule thickness of the control was thinner but still present [51]. This study indicated a direct correlation of inflammatory macrophages to the thickness of the fibrous capsule.

On the other hand, M2 macrophages have also been implicated in the formation of the fibrous capsule. M2 macrophages secrete PDGF and TGF-β, known mediators of the fibrous capsule [52]. Several studies have shown that IL-4, which causes M2 polarization, induces the formation of FBGC and subsequently the fibrous capsule [52]. A study by Kao et al. implanted a cage system subcutaneously in rats, providing a prolonged inflammatory environment [52]. Anti-murine IL-4 (IL-4Ab), murine IL-4 (muIL-4), normal goal nonspecific control IgG (gtIgG), and PBS were injected into the cages and released into the implant site to determine the effects of IL-4 on the FBR.

Implants releasing muIL-4 showed a significant increase in the formation of FBGC and fibrous capsule compared to the IL-4Ab and controls. The IL-4Ab resulted in a significantly decreased formation of FBGC and fibrous capsule compared to the controls [52].

A recent study was designed to directly assess the role of macrophage phenotype in vascularization and fibrous encapsulation of tissue engineering scaffolds [5]. Model biomaterials chosen to elicit a range of macrophage responses were implanted subcutaneously into mice for 10 days. Porous collagen scaffolds were expected to elicit an M2 response, LPS-coated scaffolds were expected to elicit an M1 response, and glutaraldehyde-crosslinked collagen scaffolds were expected to elicit a mixed M1/M2 response. Immunohistochemical analysis demonstrated that the unmodified scaffolds were surrounded by the highest numbers of M2 macrophages, indicated by three markers of the M2 phenotype, coincident with a dense fibrous capsule. The LPS-coated scaffolds were infiltrated by high numbers of M1 macrophages, as indicated by three markers of the M1 phenotype, but without evidence of fibrous encapsulation. Interestingly, the glutaraldehyde-crosslinked scaffolds stained strongly for both M1 and M2 markers, and were infiltrated by high numbers of blood vessels, in keeping with the idea that both M1 and M2 macrophages are required for vascularization [5]. Clearly, more studies are required to elucidate the relative contributions of M1 and M2 macrophages to the FBR and fibrous capsule formation.

1.4 Macrophage polarization in response to biomaterials

Understanding of the role of macrophage phenotype on the spectrum from healing to fibrous encapsulation will allow us to design biomaterials with macrophages in mind. As an initial step toward controlling macrophage behavior, several studies have systematically evaluated the response of macrophages to changing biomaterial properties.

1.4.1 Decellularized biological scaffolds

Decellularized extracellular matrix (ECM) scaffolds have a strong clinical potential to mitigate the FBR and to promote wound healing. Decellularized bladder ECM has been used to repair damaged skeletal muscle of humans, resulting in the formation of new muscle tissue, neovascularization, recruitment of endogenous myogenic progenitor cells, and functional recovery [53]. These scaffolds are prepared by removing cells and cellular debris from tissues using detergents, often followed by chemical crosslinking. Several studies have shown their potential to modulate inflammation in comparison to cellular scaffolds. Xu et al. used a primate model to show that decellularized scaffolds does not induce significant chronic inflammation or promote a severe immune response compared to the cellular scaffolds [54]. These findings are supported by the findings of Brown et al., in which the inflammatory response associated with decellularized allografts (rat body wall ECM) compared to cellular autograft (autologous body wall tissue) and porcine bladder xenografts for 28 days post implantation was examined in Sprague-Dawley rats [55]. Immunohistochemical analaysis revealed that the cellular scaffolds had a macrophage population that favored the M1

phenotype at the majority of time points, associated with a dense, poorly organized collagenous response, while the decellularized scaffolds had a macrophage population that favored the M2 phenotype, which was associated with neomatrix formation by the end of the observation period. Interestingly, only the decellularized scaffolds resulted in angiogenesis as early as three days post implantation [55]. Thus, the use of decellularized scaffolds to regenerate tissue is an active area of research [56].

1.4.2 Porosity of biomaterials

In addition to allowing for ingrowth of tissue and blood vessels, the porosity and pore diameter of a biomaterial has been shown to be critical in the FBR [20]. For example, Madden et al. showed that porous hydrogel scaffolds promoted a pro-healing response compared to non-porous biomaterials *in vivo* in two different species [20]. Microtemplated hydrogel scaffolds were fabricated from poly(2-hydroxyethyl methacrylate-co-methacrylic acid) (pHEMA-co-MAA) scaffolds with pore diameters of 20 - 80μm. Cardiac implantation of the acellular scaffolds of varying pore sizes were evaluated for 4 weeks to determine the effects of pore diameter on the formation of the fibrous capsule, neovascularization, and the macrophage phenotype profile. The non-porous scaffolds promoted a more severe inflammatory response indicated by a significantly higher expression of the M1 marker iNOS compared to the porous scaffolds. Although there was not a significant difference, there was a general increase in the expression of MMR, an M2 marker, in the porous scaffolds. In addition, the porous scaffolds with larger pores (30 - 60μm in mice and 40 - 80μm in rats) resulted in more neovascularization as indicated by significantly higher expression of RECA-1, a marker

for endothelial cells, compared to nonporous scaffolds and scaffolds with 20μm pores. At the same time, nonporous scaffolds and those with 20μm pores resulted in a significant increase in the fibrous capsule thickness. There seemed to be an optimal pore diameter of the scaffold, approximately 30-40μm, that reduced the fibrous capsule thickness and the number of M1 macrophages, and enhanced neovascularization. Interestingly, the authors noted a much higher number of macrophages expressing markers of both the M1 and M2 phenotype compared to the numbers of more homogenous populations, indicating significant contribution of hybrid phenotypes to neovascularization. This study proposed that porous biomaterials increase the activation of M2 macrophages, which coincides with enhanced vascularization of the biomaterial [20].

1.5 Active control over macrophage phenotype

With the recent increase in the number of studies examining the relationships between biomaterial properties, macrophage phenotype, and healing outcome, the possibility of controlling macrophage behavior for a beneficial response is becoming a reality. Strategies are moving away from attempts at inhibition of the inflammatory response towards those that actively work with macrophages for therapeutic effects.

Preliminary studies of drug delivery strategies that release immunomodulatory factors have shown proof-of-concept that macrophages can be harnessed. For example, the release of chemotactic factors for macrophages, including monocyte chemoattractant protein-1 (MCP1) and agonists of the S1P receptor, cause increased scaffold integration, vascularization, and tissue regeneration in cardiac and bone defects [57-59]. Mokarram

et al. evaluated the effects of macrophage phenotype manipulation via local delivery of immunomodulatory cytokines IFN- γ and IL-4 from agarose hydrogels on peripheral nerve regeneration in critical sized 15 mm sciatic nerve gap defects in rats [60]. IFN-γ, which promotes the M1 phenotype, or IL-4, which promotes the M2a phenotype, were mixed with agarose hydrogel and inserted into a hollow polysulfone tube as a nerve guidance channel and were implanted in critical nerve gap of rats for three weeks. The release of IL-4 resulted in a significant increase in the M2 macrophages and enhanced Schwann cell migration to the middle of the scaffold compared to the blank control and the release of IFN-γ. Furthermore, axon regeneration was observed in the IL-4 samples, and the amount of axons in the IL-4 samples was approximately 20 times greater than the control and IFN-γ samples. The ratio of M2 to M1 markers was linearly correlated with axon regeneration [60]. Controlled release strategies like these show that it is possible to control macrophage behavior for beneficial effects on biomaterials.

Macrophages are at the center of the FBR and consequently hold the key to the success or failure of a biomaterial. We now know that macrophage phenotype plays a critical role in determining the therapeutic outcome. More studies are required to delineate the roles of macrophage phenotype in the FBR, particularly in fibrous capsule formation vs. vascularization and integration, and the roles that biomaterials properties like surface structure and pore size play in dictating phenotypic changes. Future generations of biomaterials will consider macrophage phenotypic response as an important design consideration, and will even control macrophage behavior for beneficial outcomes.

Chapter 2: Experimental design

The overall goal of this study is to design a mathematical model to evaluate differences in normal wound healing and in macrophage dynamics in the FBR to implanted biomaterials (Figure 4). Understanding how the macrophage profile of a chronic wound deviates from normal wound healing is essential because biomaterials can then be modified to manipulate the macrophage profile for beneficial results.

The specific aims of this work are to:

1. Design and validate a mathematical model to describe macrophage polarization in normal wound healing.
2. Design and characterize model biomaterials to assess the foreign body response in vivo.
3. Apply the model to determine if the macrophage dynamics surrounding the implanted biomaterials differs from those in normal wound healing.

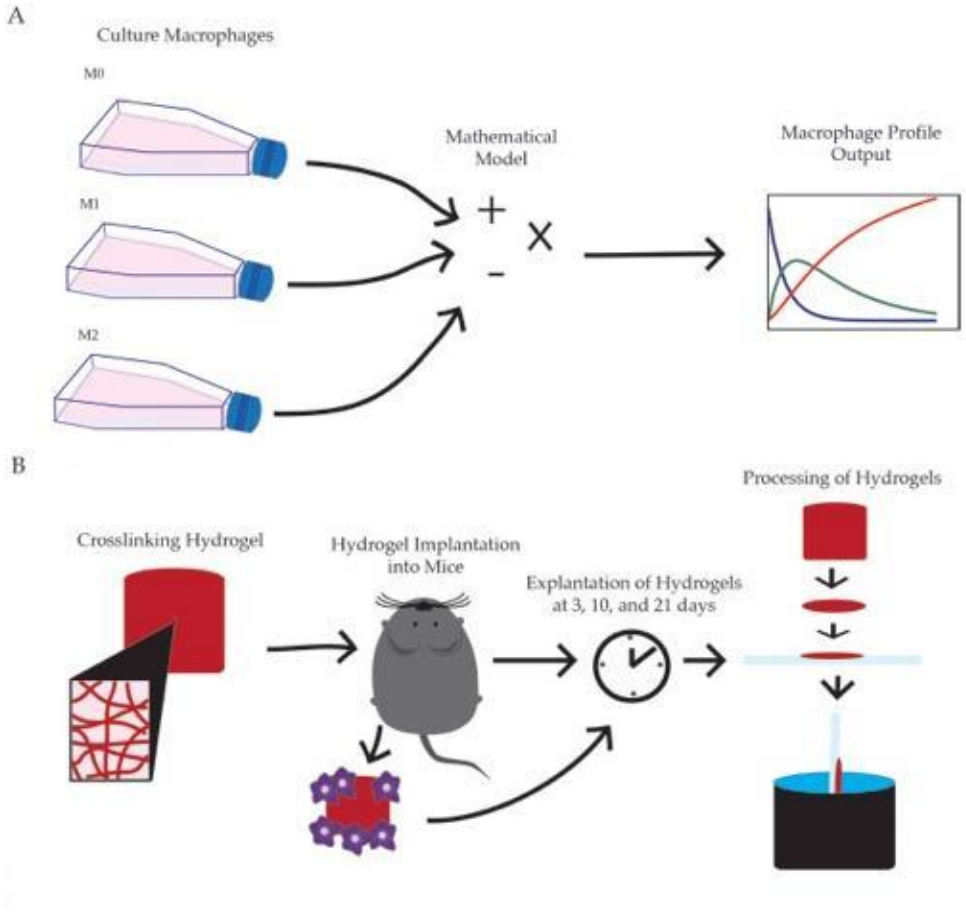

Figure 4: A schematic of the experimental design. A. The development of a mathematical model that models macrophages in normal wounding based on in vitro experiments. B. In vitro characterization of crosslinked gelatin hydrogels, which were implanted in mice at different time points to evaluate the macrophage phenotypes via histology.

2.1 Specific aim 1: Design and validate a mathematical model to describe macrophage polarization in normal wound healing

Specific aim 1 is the development of a mathematical model consisting of three ordinary differential equations of M0, M1, and M2 macrophages based on the current literature and *in vitro* experiments to represent the macrophage profile of normal wound healing (Figure 4A).

With the risks involved in the implantation of a biomaterial, animal studies are usually conducted to prove its safety and efficacy. Initially, *in vitro* studies are often done to obtain preliminary data and as proof of concept. The next logical step in evaluating a biomaterial is to use the preliminary data to design *in vivo* studies. Data from the *in vitro* and *in vivo* studies are compared side by side to validate the findings and make hypotheses of the course of behaviors when implanted into humans. However, it is difficult to precisely identify rate constants of macrophage dynamics from animal studies, because they are expensive, time-consuming, and cost animal lives. As a result, there is a need to develop a mathematical model for biomaterials based on *in vitr*o experiments to help predict the *in vivo* host response, also called the foreign body response, which will indicate the overall biocompatibility of the biomaterial [61]. Establishing this model will minimize the cost and time it takes to complete a biocompatibility study. Although there have been previous mathematical models describing the foreign body response, many of these models use parameters that are physiologically irrelevant and/or missing key biological concepts, which are critical in the foreign body response [62, 63]. The development of a mathematical model based on *in vitro* studies will help gain a better understanding the complex immune system. This knowledge can be used to help better design biomaterial devices, implants, and prosthetics to overcome this foreign body response without costly and time consuming animal studies.

2.2 Specific aim 2: Design and characterize model biomaterials to assess the foreign body response in vivo.

Specific aim 2 is the *in vitro* characterization of the model biomaterial that can be used to assess the *in vivo* foreign body response at the Shanghai Key Tissue Engineering Laboratory and compare the results to normal wound healing (Figure 4B). Gelatin hydrogels were chosen as a model biomaterial to evaluate a chronic wound caused by biomaterial implantation, which is commonly used as a model chronic wound in rodents [64, 65]. Because of the low mechanical properties of gelatin, the hydrogels were crosslinked in order to provide mechanical strength, and they were crosslinked to different extents in order to determine the effects of crosslinking on the foreign body response. The gelatin hydrogels were chemically crosslinked with glutaraldehyde (GA) to increase the mechanical stiffness. GA was chosen to chemically crosslink the hydrogels because of its ability to effectively react and bond with the primary amine groups of proteins [64, 66, 67]. Gelatin, derived from collagen, has multiple primary amine groups readily available for chemical crosslinking. The hydrogels were crosslinked at three different GA concentrations of 0.3, 0.1, and 0.05% in order to examine the effect of mechanical stiffness on the macrophage profile *in vivo*. Before the hydrogels could be analyzed in vivo, they were characterized by the hydrogel properties including the crosslinking density, mechanical properties, degradation, and swelling in order to determine any significant difference between the different concentrations of GA crosslinking.

2.3 Specific aim 3: Apply the model to determine if the macrophage dynamics surrounding the implanted biomaterials differs from those in normal wound healing.

Specific aim 3 is to assess the in vivo foreign body response in terms of the macrophage profile and the fibrous capsule surrounding the implanted hydrogels. The three different crosslinked hydrogels were implanted into C57BL/6 mice subcutaneously at three different locations per mouse at the different time points with a replica of six mice (n=6) per time point. The locations of the three hydrogels for each mouse were chosen in such a way that the concentrations of the hydrogels were in different positions for each replicate.

Immunostaining and Massson's trichrome staining were used to identify macrophage phenotypes and fibrous capsule thickness, respectively. Masson's trichrome stain is currently the standard to stain for the fibrous capsule as it stains collagen blue. The thickness of the fibrous capsule was quantified via Image J. Immunohistochemistry (IHC) was also performed to stain for the M1 and M2 macrophage phenotypes. Each sample was analyzed for the surface markers iNOS (M1 macrophages), and Arg1 and CD163 (M2 macrophages). IHC of the three surface markers stain the respective macrophages brown after development with 3,3'-diaminobenzidine (DAB). The intensity of brown staining was also quantified via Image J to determine the amount of macrophage staining in each sample. Correlation analyses were performed on the thickness of the fibrous capsule and the intensity of macrophage staining. Finally, the macrophage profiles of these biomaterial-induced chronic wounds were compared to that of normal wound healing, derived from the mathematical model developed in Aim 1.

Chapter 3: Specific Aim 1

Aim 1: Design and validate a mathematical model to describe macrophage polarization in normal wound healing.

3.1 Background and derivation

3.1.1 Existing mathematical models

A recent study by Yang et al. was conducted to mathematically model the profile of fibroblasts, macrophages, chemoattractants (TGF-B), debris cell population, and ECM production using five ordinary differential equations, which were dependent on time [63]. This study also conducted *in vivo* animal studies to compare the experimental data with the mathematical model [63]. However, only fibroblasts and macrophages were tested *in vivo*, and did not test for the production of ECM, measurement of debris population, and chemoattractants. Thus, there was no comparison of the experimental data (ECM, debris, and chemoattractants) to the developed mathematical model. Even though the modeling of fibroblasts, macrophages, and collagen/ECM is important and relevant to the foreign body response, the model did not distinguish between the different macrophage phenotypes of M1 or M2, which are essential in the foreign body response. Modeling of the M1 and M2 macrophages and performing histology to quantify the collagen production would have made this mathematical model more accurate and physiological relevant.

Another study by Wang et al. developed a mathematical model for macrophage activation in left ventricular remodeling in post-myocardial infarction [62]. In this

mathematical model, the M0, M1, M2, and three cytokine productions (IL-10, TNF-a, IL-1) were modeled using six ordinary differential equations [62]. These equations are more physiologically relevant because it took into account the different macrophage phenotypes and the transitions from the M1 to M2 phenotype. However, many of these parameter values were estimates derived from other models that may not be relevant and were not based on any *in vitro* or *in vivo* experiments. In addition, immunostaining of the different macrophage phenotypes in post-myocardial infarction was not performed resulting in no comparison to any experimental data to validate the model. The macrophage profile in post-myocardial infarction may or may not be different from that of normal wound healing. Macrophage staining should have been performed in this study for verification.

3.1.2 Biology of mathematical model

A mathematical model of the macrophage profile in normal wound healing was established by developing three ordinary differential equations (ODE) to describe the three main macrophage populations (M0, M1, M2), influenced by understanding of macrophage biology. Based on the current literature, it is known that there are tissue resident macrophages residing in the body [68]. In response to an injury, circulating monocytes derived from the bone marrow are recruited to the injury site and differentiate into unactivated macrophages (M0) [69]. The initial inflammatory response and environmental stimulus polarizes the M0 to the M1 phenotype resulting in a relatively high amount of M1 during the early stage of wound healing. As the inflammatory phase

diminishes and the wound heals over time, the M1 decreases while the M2 begins to accumulate. During the wound healing process, the macrophages are either removed from the system to the lymph nodes [38] or die at the wound site, which is called the death rate. The accumulated macrophages eventually migrate to the draining lymph nodes returning back to the pre-injury state of resident macrophages after the wound is completely remodeled and healed [68].

3.1.3 Criteria for mathematical model

Based on the known temporal sequence of macrophage appearance and disappearance following injury, the successful mathematical model of the macrophage profile must meet these specific criteria:

1. A cellular infiltration of M1 macrophages initially dominates the early stage of wound healing representing the inflammatory response with a peak about 3-5 days post-injury [36, 42].
2. Following the inflammatory response, the M2 macrophages accumulate, eventually dominating the M1 macrophages, which represents the proliferation and remodeling stages of wound healing, with a peak at approximately 10 days [37, 70].
3. Macrophage accumulation levels return back to pre-injury state of resident macrophages after the wound the completely healed and remodeled [68].

3.1.4 Assumptions

Some assumptions were made in order to simplify this model:

1. The rate constants were calculated from the rate of polarization, transition, or proliferation at particular time points from experiment of primary human macrophages cultured in vitro. The rate constants were assumed to be the same throughout the wound healing process.
2. Only the M2 macrophages proliferate, which has been shown before [37] and which we also found, in that the increase in the cell viability from day 3 to day 6 was only seen in the M2 population [76].
3. The only source of M1 and M2 macrophages is the polarization of M0 or the transition of M1 to M2.
4. M1 and M2 macrophages do not dedifferentiate back to the M0 macrophages because environmental stimuli are constantly present.
5. M2 macrophages do not transition back to M1 macrophages.
6. The macrophage profile is only representative of recruited macrophages and not resident macrophages. The baseline of 0 macrophages is indicative of resident macrophages.

3.1.5 Mathematical model derivation

The rate of macrophage accumulation is governed by the following general equation:

$$input - output + generation = accumulation \quad \textbf{(1)}$$

Based on the macrophage biology described above, the input of this system is the polarization or transition from the initial population that enters the system, while the output is polarization to a different phenotype and the death rates of each population, and the generation term represents the rate of proliferation of the macrophages. The net rate of the three terms equals the rate of accumulation, which represents the change in the amount of macrophages of each phenotype at any given point in time.

Rate equations were formulated to describe macrophage polarization to a new phenotype. The rate equations are given by the following:

$$M0 \xrightarrow{k1} M1 \quad \textbf{(2)}$$

$$M0 \xrightarrow{k2} M2 \quad \textbf{(3)}$$

$$M1 \xrightarrow{k3} M2 \quad \textbf{(4)}$$

$$M2 \xrightarrow{k4} pM2 \quad \textbf{(5)}$$

where *k1* is the rate at which M0 polarizes to the M1, *k2* is the rate at which M0 polarizes to the M2, *k3* is the rate at which M1 polarizes to the M2, *k4* is the self-proliferation rate of M2, and pM2 is the proliferated M2 macrophages. Equations 2-4 can be rewritten in terms of differential equations:

$$\frac{dM1}{dt} = k1 * M0 \quad \textbf{(6)}$$

$$\frac{dM2}{dt}(from\ M0\ polarization) = k2 * M0 \quad \textbf{(7)}$$

$$\frac{dM2}{dt}(from\ M1\ transition) = k3 * M1 \quad \textbf{(8)}$$

where equation 6-8 represent the rate of M1 polarization from M0, rate of M2 polarization from M0, and rate of M2 transition from M1, respectively.

From the rate equations and the death rates obtained from the *in vitro* experiments, the rates of the inputs and output of each phenotype were derived. More specifically, the macrophages within the M0 population will either polarize to the M1 or M2 phenotype. Thus, the output is the rate at which the M0 polarizes to M1 or M2 or the removal of the M0 macrophages to the lymph node/cell death, derived from (2) and (3), is:

$$M0\ output = (k1 * M0) + (k2 * M0) - (d0 * M0) \quad \textbf{(9)}$$

where *d0* is the death rate constant of M0 population. Similarly, the surviving macrophages within the M1 population will transition to the M2 phenotype. The output of M1, derived from (4), is:

$$M1\ output = (k3 * M1) - (d1 * M1) \quad \textbf{(10)}$$

where *d1* is the death rate constant of M1 population.

The output of the M2 population is given only by the death rate:

$$M2\ output = (d2 * M2) \quad \textbf{(11)}$$

where *d2* is the death rate constant of the M2 population.

The input of M0 is the migration of macrophages from the circulating blood from the body to the wound site (D).

$$M0\ input = D \quad \textbf{(12)}$$

The input of the M1 population is the rate at which the surviving M0 macrophages are polarized to the M1, derived from (2):

$$M1\ input = k1 * M0 \quad \textbf{(13)}$$

The input of M2 is the rate at which the surviving M0 polarizes to the M2 and the surviving M1 transition to the M2, derived from (3) and (4):

$$M2\ input = (k2 * M0) + (k3 * M1) \quad \textbf{(14)}$$

Both the M0 and M1 populations do not consist of a generation term because both of these macrophage populations were assumed to not proliferate based on the fact that there was no observable proliferation in the *in vitro* experiments. The generation of the M2 is the proliferation rate of the surviving M2 population, derived from (5).

$$M2\ generation = k4 * M2 \quad \textbf{(15)}$$

where *k4* is the proliferation rate constant of the M2 population.

The mathematical model is a closed system of a specific amount of macrophages at the initial conditions, which represent the amount of macrophages that are recruited to the system. Since it is assumed that the M1 and M2 macrophages originate from the M0 macrophages, the initial conditions of M1 and M2 are zero, and only the M0 are recruited or migrate to the system at t=0.

The rate of accumulation or amount of macrophages for each population can be computed by combining the terms according to (1). Thus, the rates of change of M0, M1, and M2 are shown below:

$$\frac{dM0}{dt} = D + (-k1 * M0) + (-k2 * M0) - (d0 * M0) \quad \textbf{(16)}$$

$$\frac{dM1}{dt} = (k1 * M0) + (-k3 * M1) - (d1 * M1) \quad \textbf{(17)}$$

$$\frac{dM2}{dt} = (k2 * M0) + (k3 * M1) + (k4 * M2) - (d2 * M2) \quad \textbf{(18)}$$

These three ordinary differential equations were modeled using ode45 function in MATLAB.

3.2. Methods

3.2.1. *In vitro* experiments for mathematical model

Data for the mathematical model were derived from previously published *in vitro* experiments by our group [76] (reproduced below for clarity), and were used to determine physiologically relevant parameters and their respective values. Unactivated and polarized macrophages were characterized by cell viability and flow cytometry.

3.2.1.a Cell viability of macrophage phenotypes

Briefly, monocytes were isolated from leukocyte fraction of human peripheral blood using sequential Ficoll and Percoll density gradient centrifugation, as previously described [5]. Monocytes were cultured in at 37ºC and 5% CO_2 in ultra-low attachment flasks in complete media with macrophage colony stimulating factor (MCSF) for 5 days to differentiate to unactivated macrophages (M0). M0 macrophages were seeded and cultured at a density of $1.0x10^6$ cells/ml at day 0. Macrophages were polarized over the next 1-6 days via IFN-γ and lipopolysaccharide (LPS) for M1 and IL-4 and IL-13 for M2, with M0 as control and a change in media at day 3. During the media change, MCSF, M1, and M2 polarizing media was added to its respective phenotype. In addition, the media of the M1 group switched to M2 polarizing media in order to determine the rates that the macrophages transition [5]. Cell viability of the macrophages was determined at each day via trypan blue exclusion. Macrophages at each time point were characterized by expression of M1 (CCR7) and M2 (CD206) surface markers via flow cytometry.

3.2.1.b. Flow cytometry of macrophage phenotypes

The initial condition values were obtained from the *in vitro* experiment explained above [76]. Thus, the initial condition values for M0, M1, and M2 are $1.0x10^6$, 0, and 0 cells, respectively. The macrophage saturation was determined to be the same value as the initial condition of M0 so that the total amount of macrophages cannot exceed the initial amount of macrophages recruited, simplifying the model. Other parameter values were also calculated from flow cytometry and cell viability analysis. M1 and M2 macrophages were identified by the surface marker expression of CCR7 and CD206, respectively. To describe the change in the numbers of cells representing the M1 and M2 populations, the data has been gated based on the mean intensities of CD206 and CCR7 expression of the M0 population at the same time point. In order to determine the number of macrophages in each population, cells were described as $CCR7^{hi}CD206^{lo}$, which would indicate the M1 phenotype, and as $CCR7^{lo}CD206^{hi}$, indicative of the M2 phenotype. The percentage of macrophages expressing each marker was calculated based on these thresholds. Macrophages in each population that were not $CCR7^{hi}CD206^{lo}$ or $CCR7^{lo}CD206^{hi}$ were considered to be M0 macrophages.

3.3 Results

3.3.1 *In vitro* experiments for mathematical model

3.3.1.a Cell viability of macrophage phenotypes

The cell viability of the macrophage populations is reported as the fold change over the initial concentration (Table 1, Figure 5) [76]. A decrease in the macrophage

populations was observed from day 1 to day 3 indicating cell deaths within each population. At day 3, the media was changed replenishing the nutrient uptake. The number of M0 and M1 macrophages leveled off from day 4 to day 6. However, an increase in the M2 macrophages was observed from day 4 to day 6, which indicates proliferation. Therefore, it was assumed that only the M2 macrophages proliferate, which is in agreement with recent publications [37].

Table 1: The raw data of the cell viability of the concentration (cells/mL) of each macrophage population [76]

Cell Viability (10^6 cells/mL)	M0	M1	M2	M1 -> M2
Day 1	1	0.95	1	N/A
Day 2	0.566	0.633	0.666	N/A
Day 3	0.6	0.49	0.255	0.49
Day 4	0.4	0.326	0.17	0.733
Day 6	0.458	0.333	0.625	0.575

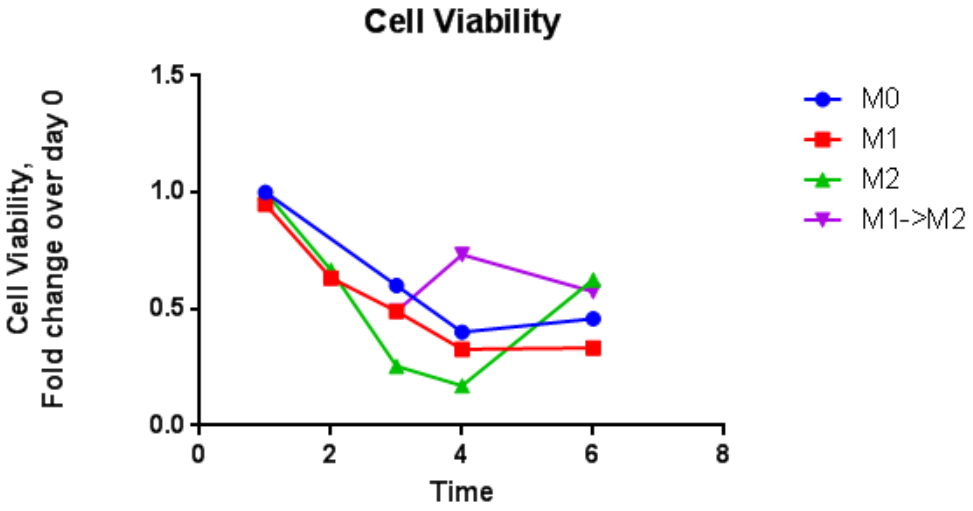

Figure 5: Cell viability calculated by the fold change over day 0 of each macrophage population [76]

Table 2: The raw data of flow cytometry as reported as the percentage of positive cells that express M1 or M2 characteristics for each macrophage phenotype [76]

% Positive Cells	Macrophage Phenotype	M0	$CCR7^{hi}/CD206^{lo}$ (M1)	$CD206^{hi}/CCR7^{lo}$ (M2)
Day 0	M0	59.31	3.09	37.6
Day 1	M0	62.59	7.51	29.9
	M1	52.95	42.3	4.75
	M2	52.65	4.65	42.7
Day 2	M0	56	14	30
	M1	58.49	33.2	8.31
	M2	46.6	12.9	40.5
Day 3	M0	52	31	17
	M1	55.88	34.8	9.32
	M2	33.7	26.8	39.5
Day 4	M0	63.6	11.1	25.3
	M1	37.36	61.4	1.24
	M2	11.28	0.82	87.9
	M1 -> M2	72	13.1	14.9
Day 6	M0	61.1	11.4	27.5
	M1	35.53	63.6	0.863
	M2	36.15	6.75	57.1
	M1 -> M2	21.61	1.09	77.3

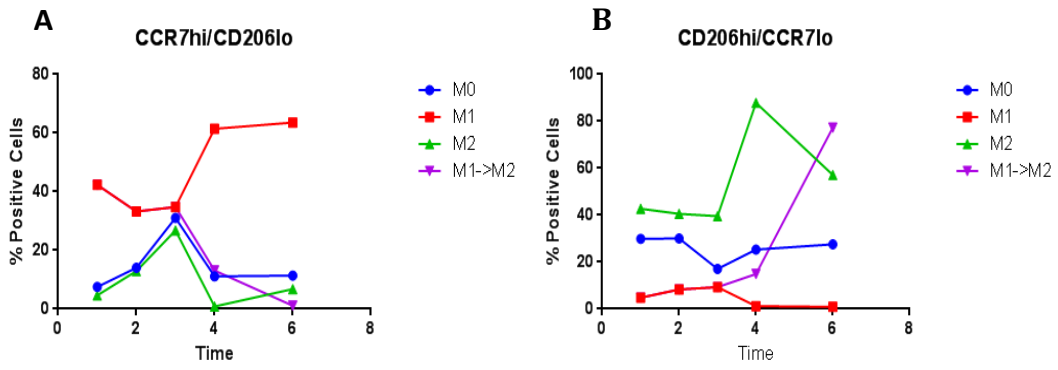

Figure 6: The macrophage expression of M1 and M2 characteristics in flow cytometry [76]

3.2 Determination of parameter values

To calculate the death rates, the cell viability and the percent expression of the marker from flow cytometry were multiplied for a more accurate representation of the expression of each of the surviving macrophage population. Cell viability provides information about the size of the population but does not indicate the phenotypic distribution within that population. On the other hand, flow cytometry indicates the phenotype expression, but does not show the cell survival or death from each time point. Therefore, the product of the two, termed the survival expression, gives a better representation of the rates of each of the macrophage population (Table 3). The values of death and proliferation rates constants were determined by first calculating the rate or slope of the survival expression at day 1 to day 3 of the respective macrophage population as seen in equation 19, as an approximation of the rate at day 1. This rate was then divided by the initial population at day 1 of the respective phenotypes in order to calculate the rate constant. For example, *d0* was calculated by the following steps: the

quantity of the difference of the survival expression of the M0 population from day 1 to day 3 was divided by the quantity of the difference in time, in this case, from day 1 to day 3. The rate constant *d0* is determined by dividing the calculated rate/slope by the population of M0 at day 1. *d1* and *d2* were calculated similarly, but within the M1 and M2 populations, respectively.

The rate of change or the slope is calculated in the following equation:

$$\frac{d}{dt} = \frac{Survival\ Expression_2 - Survival\ Expression_1}{Time\ (Day_2 - Day_1)} = rate\ constant * population \qquad \textbf{(19)}$$

Similarly, the M2 proliferation rate was also calculated using the survival expression from day 3 to day 6.

The rates of macrophage polarization from M0 to M1 and M2 were determined by the survival expression of the phenotype when initially stimulated with cytokines at day 0. The rate of change of the amount of macrophages expressing the phenotype from day 0 to day 1 was determined to calculate the polarization rates. Similarly, the transition rate from M1 to M2 was determined by the following steps. The rate of change of the increase in survival expression of M2 macrophages and the rate of change of the decrease in the survival expression of M1 macrophages of the M1 -> M2 group from day 3 to day 6 were calculated and averaged to obtain the M1 to M2 transition rate.

The rate constant *k1* was calculated using a similar method to that of the death and proliferation rates by first determining the rate of polarization from day 0 to day 1 using equation 6. The difference between the survival expression of $CCR7^{hi}CD206^{lo}$ of the M0 population at day 0 and the survival expression of $CCR7^{hi}CD206^{lo}$ of the M1 population at day 1 was calculated and dividing by the quantity by the difference in time,

in this case, from day 0 to day 1, as an approximation of the rate of polarization at day 1. The resulting calculation is the rate of M1 polarization from M0. From equations 6, *k1* was calculated by dividing the rate of M1 polarization by the average population of M0 at day 1. The average population of day 0 and day 1 was chosen because the rate was calculated between these two time points was not measured in flow cytometry or cell viability. Similarly, the rate constant *k2* was calculated by determining the rate of M2 polarization from the M0 population using equation 7. The difference between the expression of $CCR7^{lo}CD206^{hi}$ of the M0 population at day 0 and the expression of $CCR7^{lo}CD206^{hi}$ of the M2 population at day 1 was calculated and dividing that quantity by the difference in time. From equation 7, *k2* was calculated by dividing the rate of M2 polarization by the average population of M0 between day 0 and day 1. This time period was chosen because the M1 and M2 cytokines were added at time 0 to polarize the M0 macrophages to each phenotype, and they appear to be fully differentiated at the next time point, based on flow cytometry data.

To calculate the M1 to M2 transition rate constant *k3*, the rate of increase in the expression of $CCR7^{lo}CD206^{hi}$ of the M2 population and the rate of decrease in the expression of $CCR7^{hi}CD206^{lo}$ of the M1 population were averaged from day 3 to day 6 using equation 8. The proliferation of M2 rate constant *k4* was determined by calculating the rate of the survival expression of $CCR7^{lo}CD206^{hi}$ of the M2 population from day 3 to day 6. Day 3 was chosen as the initial time point because the M2 macrophages appeared to start proliferating at this time, based on cell viability data.

Table 3: **The survival expression of each of the macrophage populations**

Survival Expression (cells)	Macrophage Phenotype	M0	$CCR7^{hi}/CD206^{lo}$	$CD206^{hi}/CCR7^{lo}$
Day 0	M0	59.31	2.93	37.6
Day 1	M0	62.59	7.13	29.9
	M1	52.95	40.18	4.75
	M2	52.65	4.41	42.7
Day 3	M0	31.2	18.6	10.2
	M1	27.3	17.0	4.56
	M2	8.59	6.83	10.0
Day 6	M0	28.0	5.22	12.6
	M1	11.8	21.2	0.28
	M2	22.5	4.21	35.6
	M1 -> M2	12.4	0.626	44.4

Table 4: **The rate constants that were calculated by the survival expression term**

Death and proliferation rate constants	Value (day^{-1})
d0 (day 1 to day 3)	0.156
d1 (day 1 to day 3)	0.121
d2 (day 1 to day 3)	0.163
k4 (day 3 to day 6)	0.0853

Table 5: **The polarization and transition rates of each of the macrophage population**

Polarization and transition rates	Value (per day)
k1 (day 0 to day 1)	0.611
k2 (day 0 to day 1)	0.0836
Decrease M1 (M1 -> M2, day 3 to day 6)	0.114
Increase M2 (M1 -> M2, day 3 to day 6)	0.0547
k3 (M1 -> M2, day 3 to day 6)	0.0846

Table 6: List of all the parameters with its respective values of the mathematical model

Parameter	Description	Value	Source
D	M0 migration to wound site	0.015 cell/day	[63]
d0	M0 death rate	0.156 /day	Figure 5, 6
d1	M1 death rate	0.121 /day	Figure 5, 6
d2	M2 death rate	0.163 /day	Figure 5, 6
k1	M0 transition to M1	0.611 /day	Figure 5, 6
k2	M0 transition to M2	0.0836 /day	Figure 5, 6
k3	M1 transition to M2	0.0846 /day	Figure 5, 6
k4	M2 proliferation	0.0853 /day	Figure 5, 6

The M0, M1, and M2 macrophage profiles of normal wound healing were modeled in MATLAB using ode45 (Figure 7).

3.3.3 Results: Model of macrophage profile in normal wound healing

Upon injury or the start of the model, the majority of the M0 macrophages are polarized to the M1 phenotype while some to the M2 phenotype because the M0 macrophages are mainly exposed to inflammatory cytokines and environment. According to the model, the M1 macrophages rapidly increase and peak at day 5 post-injury, but gradually decrease afterwards. The early infiltration of the M1 macrophages is required for clearance of wound debris. After day 5, the M1 macrophages transition to the M2 phenotype representing a switch to the pro-healing or anti-inflammatory stage of wound

healing. The M2 macrophages, from the start of the injury or model, gradually increase and accumulate and are eventually the dominant phenotype in the system. In addition to the polarization of M0 to M2 and the transition of M1 to M2, the M2 macrophages also proliferate. The macrophages at this stage are responsible for tissue regeneration and remodeling. After the wound is remodeled and healed, the macrophages return back to the pre-injury level of resident macrophages. Thus, this model accurately represents the macrophage profile observed in normal wound healing [36, 70, 71].

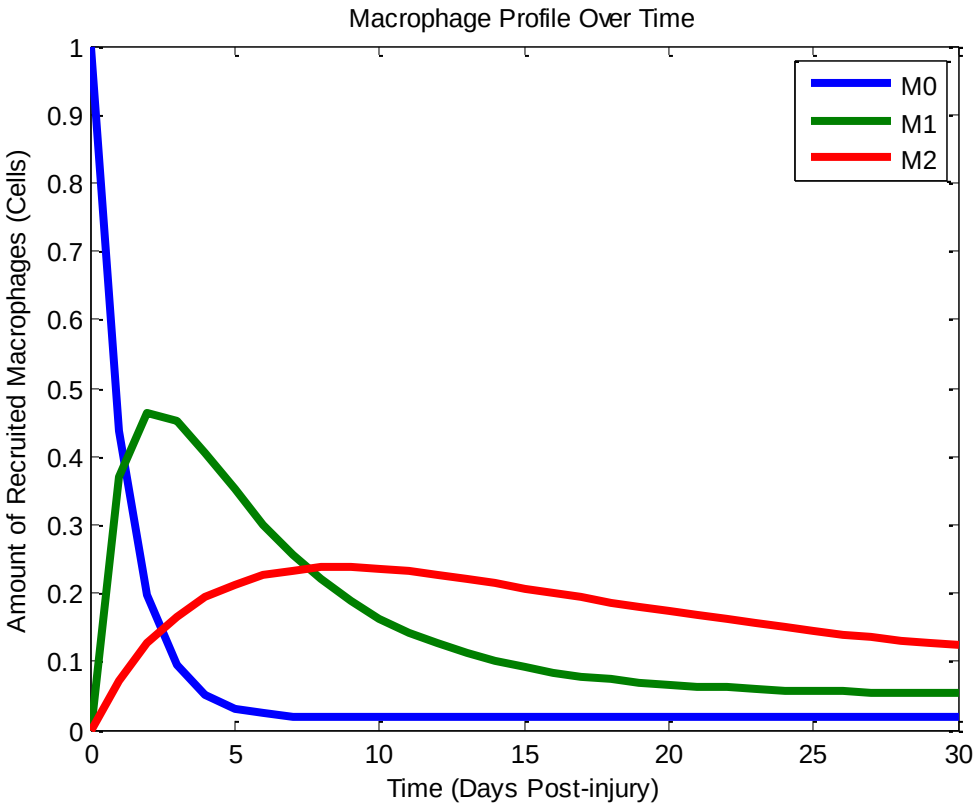

Figure 7: The output of the model representing M0, M1, and M2 macrophage profile in normal wound healing.

Chapter 4: Specific Aim 2

Aim 2: Design and characterize model biomaterials to assess the foreign body response in vivo.

4.1. Design criteria

The criteria for this specific aim is to determine the concentration of GA required to crosslink the gelatin hydrogel that would result in hydrogel properties that are statistically different such as the stiffness. The crosslinked hydrogels were characterized by four different properties in order to determined significant differences between the hydrogels. The four characterization properties include mechanical stiffness, degradation, swelling, and crosslinking density.

4.2 Methods

4.2.1. Preparation of glutaraldehyde and glycine

Glutaraldehyde (25% stock solution) from Sigma Aldrich was diluted with phosphate buffer saline (PBS) to 0.05%, 0.1%, and 0.3% concentrations. 0.1 M glycine (Sigma Aldrich) was made by dissolving 0.225 g of glycine in 30 mL of sterile PBS. The glycine solution was then sterilized via heating and UV light for at least 2 hours.

4.2.2 Preparation of sodium citrate and sodium phosphate

Sodium citrate (Sigma Aldrich) was made by dissolving 2.94 g of sodium citrate tribasic in 1000 mL of DI water. The pH was of the solution was adjusted to 6.0 by adding approximately 200 uL of 37% hydrochloric acid. 0.5 mL of Tween-20 (Sigma

Aldrich) was added to the solution and mixed well. Sodium phosphate (Sigma Aldrich) was made by dissolving 1.2 g of sodium phosphate monohydrate in 1000 mL of PBS and adding 0.1 mL of Tween-20.

4.2.3. Preparation of crosslinked gelatin hydrogels

10 wt% gelatin was made by heating and dissolving 4 g of gelatin (Sigma Aldrich, Type B bovine skin) in 40 ml of PBS. 8 mL of the gelatin solution was transferred into petri dishes and allowed to cool to room temperature. The petri dishes were placed in a refrigerator or ice bucket in order for the gelatin to completely solidify. Once solidified, a 5 mm biopsy punch was used to punch the gelatin into cylindrical disks. The gelatin hydrogels were crosslinked by immersion in 0.05%, 0.1%, and 0.3% GA solutions in a shaker overnight. The crosslinked gelatin hydrogels were then sterilized under UV light for at least 2 hours. The hydrogels were then washed 4 times in PBS for 15 minutes each wash. Afterwards, the hydrogels were put into 0.1M glycine solution in a shaker overnight to neutralize any residual GA. The hydrogels were washed an additional two times in PBS for 15 minutes each. Again, the hydrogels were sterilized under UV light for at least 2 hours.

4.2.4 Hydrogel characterization

4.2.4.a Mechanical testing and Young's modulus of hydrogels

The crosslinked gelatin hydrogels were mechanically tested via compression tests in order to determine the effects of crosslinking. The force and displacement data were

obtained via Bose Electroforce 3100 Test Instrument of Drexel University for each of the hydrogel samples. Using a caliper, the dimensions, the height and the diameter, of the hydrogels were measured. The hydrogels were compressed to 30% strain at a rate of 0.333 per second. The stress and strain were calculated, and the slope of the initial linear region, about 5-7% strain, was used to determine the Young's modulus.

4.2.4.b Degradation of gelatin hydrogels

Crosslinked hydrogels were immersed for one week in collagenase (Sigma Aldrich) to monitor enzymatic degradation. The concentration of collagenase was 5 ug/mL. The initial mass of the hydrogels were measured, and then the hydrogels were massed every 24 hours after blotting dry on a paper towel to determine the percent mass loss over time.

4.2.4.c Swelling ratio of hydrogel

The swelling ratio of the hydrogels was calculated by the following equation:

$$Swelling\ Ratio = \frac{w_s - w_d}{w_d} \quad \textbf{(20)}$$

where w_s is the swollen weight and w_d is the dry weight. The swollen weight was calculated by measuring the mass of the hydrogels after allowing them to reach equilibrium after swelling in PBS overnight. The hydrogels were then allowed to dry at room temperature in order to measure the dry weight.

4.2.4.d Crosslinking density of hydrogels

The crosslinking density of each hydrogel was calculated by the modified Flory Rehner equation [72]:

$$\frac{-[\ln(1-v_p)+v_p+\chi*v_p^2]}{\rho*V_1*(v_p^{\frac{1}{3}}-\frac{v_p}{2})} = \varepsilon \quad \textbf{(21)}$$

where ε is the crosslinking density, v_p is the polymer volume fraction, χ is the polymer-solvent interaction parameter, ρ is the density of the polymer, and V_1 is the molar volume of solvent. v_p was calculated by the measuring the dimensions of the hydrogels. χ was determined via literature search [72]. The density of the hydrogel was calculated by measuring the mass of the hydrogel divided by the volume of the hydrogel. V_1 was calculated by determining the molar mass of H_2O. The crosslinking density was calculated with the given parameters from experiments (v_p, ρ) and literature.

4.2.5 Statistical analysis

Statistical analysis was performed in MATLAB using one-way ANOVA with Tukey post hoc analysis in order to determine statistical significance between the crosslinked hydrogels.

4.3 Results

4.3.1 *In vitro* hydrogel characterization

The crosslinked gelatin hydrogels were characterized by mechanical testing, degradation, swelling, and crosslinking density. As seen in the figures below, the values

obtained for the hydrogels of the three different crosslinking concentrations were statistically different from each other in each of the experiments.

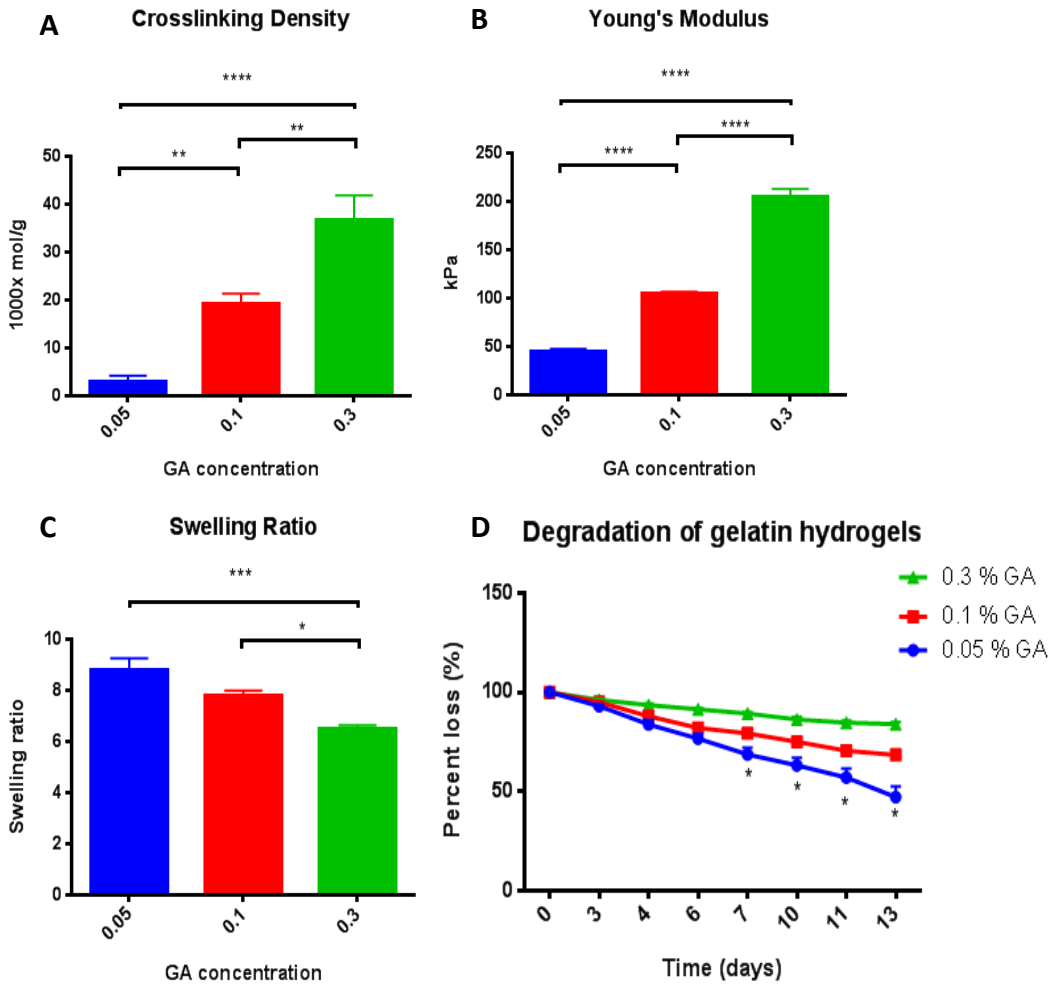

Figure 8: The crosslinked hydrogels characterized by the hydrogel properties. A. The crosslinking density of each hydrogel is significantly different. B. The stiffness of each hydrogel is significantly different. C. The 0.3% hydrogel was significantly different from the other two hydrogels. D. The degradation of each hydrogels were significantly different from day 7 to day 13. * indicates statistical significance ($p<0.05$) between the indicated groups. ** denotes $p<0.01$, * denotes $p<0.005$, **** denotes $p<0.001$**

As expected, the crosslinking density of the hydrogels increased as the concentration of GA increased. From the ANOVA analysis, the three hydrogels (0.5%, 0.1%, and 0.3%) were statistically significant from each other with $p < 0.05$. Similarly, the Young's modulus of the hydrogels increased with increasing crosslinking, and the hydrogels were all significantly significant from each other. The swelling ratio of the hydrogels decreased with increasing crosslinking, which has been shown before [72]. With a network of crosslinks, hydrogels cannot absorb as much water compared to less crosslinked hydrogels, thus reducing the swelling of the hydrogels. The swelling ratio of both the 0.05% and 0.1% crosslinked hydrogel was significantly lower than that of the 0.3% crosslinked hydrogel. The 0.05% and 0.1% hydrogels were statistically similar. In addition, the rate at which the hydrogels degraded decreased with increasing crosslinking. The hydrogel crosslinked at a higher concentration resulted in a slower degradation because of more crosslinks and bond formed within the network structure.

Chapter 5: Specific Aim 3

Aim 3: Apply the model to determine if the macrophage dynamics surrounding the implanted biomaterials differs from those in normal wound healing.

5.1. Experimental design

Three crosslinking concentrations were chosen to represent biomaterials with high, medium, and low crosslinking. Consequently, the crosslinking of the hydrogels affects the hydrogel properties including degradation, swelling, and mechanical stiffness. The 0.05, 0.1, and 0.3% GA crosslinked hydrogels were determined to be statistically

different in crosslinking density, mechanical stiffness, degradation, and swelling ratio from each other. Thus, these hydrogels can be implanted subcutaneously in mice to assess the FBR in response to the different biomaterial properties. Each of the three hydrogels was implanted subcutaneously at three different location of the back of one mouse in order to avoid the difference in immune responses of different mice. A replica of 6 (n=6) mice was used to determine statistical significance. In addition, the three hydrogels in each mouse were implanted at three different time points of 3 days, 10 days, and 3 weeks. The three time points were chosen to assess the FBR of a chronic wound over time representing the inflammatory stage, the proliferative stage, and the remodeling stage.

5.2 Methods

5.2.1 *In vivo* implantation subcutaneously in mice

All animal experiments were conducted in accordance with the local ethical committee of Shanghai Jiao Tong University. C57BL/6 6-8 week old male mice were ordered from Shanghai 9th People's Hospital. The mice were anesthetized with choral hydrate and shaved prior to surgery. The hydrogel samples were implanted subcutaneously in the mice. Three incisions were made on each mouse with scissors to implant the three different concentrations of crosslinked gelatin hydrogels (Figure 10). The first incision was made at the top of the back body, right below the neck. The second incision was made on the left side of the back body, next to the left back legs. The third and final incision was made on the right side of the back body, next to the right back legs.

After each incision, a pocket was made under the skin with forceps. The wound was sutured together after the hydrogels were implanted. The mice were monitored daily to observe for any signs of infections or abnormalities. Six mice (n=6) were used for each time point.

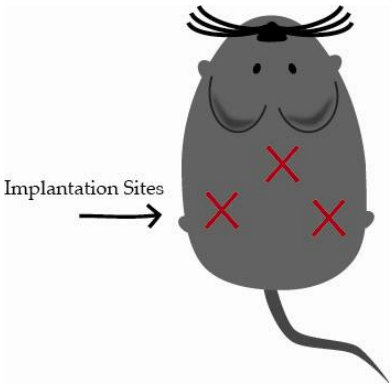

Figure 9: A schematic of the locations in which the crosslinked hydrogels were implanted subcutaneously per mice. A hydrogel with different crosslinking concentration was implanted for each location.

5.2.2 Explanting and paraffin embedding samples and sectioning

Explanting and paraffin embedding was performed at Shanghai Key Tissue Engineering Laboratory of Shanghai Jiao Tong University. Sectioning was performed at Kimmel Cancer Center (KCC) of Thomas Jefferson University. After each timepoint (3 days, 10 days, and 3 weeks), the mice were euthanized and the hydrogels were explanted. Upon explanting, the hydrogels were attached to the skin by the fibrous capsule around the hydrogel. The hydrogels and the surrounding tissues were cut and immediately fixed in 4% (PFA) for 24 hours. Once fixed, the hydrogels were washed for 8 hours in PBS. The samples then underwent dehydration and xylene replacement through an alcohol and xylene series to remove any water remaining in the sample. The samples were then

embedded in a block of hot paraffin and allowed to cool overnight. Each sample embedded in paraffin was placed in ice for 30 minutes prior to microtome sectioning for smoother sectioning. The samples were then sectioned at 5 um. Two different sections of each sample were put on glass slides for staining.

5.2.3 Histological analyses

The sectioned samples were prepared for histological analyses including H&E, Masson's trichrome, and IHC staining. Once the fibrous capsule and macrophage expression were quantified, correlation analyses were performed to determine the relationships between the macrophage phenotype and the fibrous capsule.

5.2.3.a Deparaffinization of sectioned samples

The sectioned samples on the slides were put on a slide rack and placed in an oven at 70C for 45 minutes to melt the paraffin wax. The slide rack was then immediately immersed in 100% CitriSolv (Sigma Aldrich) for 5 minutes. The slide rack was then immersed in the following order and duration: 100% CitriSolv for 5 minutes, 100% CitriSolvfor 5 minutes, 100% ethyl alcohol for 1 minute, 100% ethyl alcohol for 1 minute, 95% ethyl alcohol for 1 minute, 95% ethyl alcohol for 1 minute, and 80% ethyl alcohol for 1 minute. The slides were then rinsed with water.

5.2.3.b H&E staining

After deparaffinization of the samples, the slide rack was immersed in a solution of hematoxylin (Sigma Aldrich) for 3 minutes. The slides were then rinsed in a water

bath, followed by immersing the slide rack in a hydrochloric acid/alcohol mixture (Sigma Aldrich) for 1-3 seconds. Next, the slides were immersed in a water bath for 20 minutes. The slides were dipped in eosin (Sigma Aldrich) for 15 seconds. The slides were then dehydrated again through an ethanol series. Lastly, two drips of Permount (Sigma Aldrich) and a cover slip was added to preserve each of the sectioned samples.

5.2.3.c Masson's trichrome staining

Masson's trichrome kit was purchased from Sigma Aldrich. After deparaffinization of the samples, the tissue samples in the slide rack were re-fixed in Bouin's solution for 1 hour at 56 °C and were washed in running tap water for 7 minutes to remove the yellow color afterwards. The samples were then immersed in hematoxylin solution for 1 minute and were washed in running warm tap water for 10 minutes. The samples were rinsed in deionized (DI) water and immersed in Biebrich scarlet-acid fuchsin solution for 13 minutes. The samples were washed again in DI water and differentiated in a solution of phosphomolybdic-phosphotungstic acid for 20 minutes or until the collagen was not stained red. The samples were transferred directly to aniline blue solution for 12 minutes and rinsed with DI water. Afterwards, the samples were immersed in 1% acetic acid solution for 5 minutes and rinsed in DI water. To preserve the samples using Permount, the samples were dehydrated through a series of ethyl alcohol concentrations and CitriSolv as described above. Two drops of Permount and a coverslip were added to preserve the stained samples.

5.2.3.d Immunohistochemistry staining

After deparaffinization of the samples, antigen retrieval was performed in order to unmask and expose the antigen site from the crosslinks when fixed with PFA. The samples were immersed in 10mM sodium citrate (Sigma Aldrich) and placed in a microwave and heated until boiling. The samples were kept in the solution inside the microwave for 20 minutes and were cooled to room temperature and washed with running tap water afterwards. BLOXALL solution of the ImmPress Excel staining kit (Vector Laboratories) was added in order to block any endogenous peroxide in each sample. The samples were then washed in the buffer 2x for 5 minutes each. 2.5% normal horse serum was added and incubated for 20 minutes to block the samples. The primary antibodies iNOS (Abcam, rabbit anti-mouse), Arg1 (Santa Crus Biotechnology, goat anti-mouse), and CD163 (Santa Cruz Biotechnology, rabbit anti-mouse) were added to the samples and incubated overnight at 4 C. The samples were washed 2x in buffer solution for 5 minutes each. The ImmPress Excel secondary antibody (horse anti-rabbit or horse anti-goat) was then added to the samples and incubated for 45 minutes. The samples were washed 3x in buffer solution for 5 minutes each. DAB reagent 1 and DAB reagent 2 was mixed together to make the final DAB solution. Following the wash, DAB was added to the samples with the same amount of time for each sample. The samples were washed in the buffer solution for 2x for 5 minutes each and then rinsed in tap water. The samples were immersed in hematoxylin as a counterstain for about 10 seconds and were washed

in running tap water for 5 minutes. The samples were dehydrated through a series of ethanol and Citrisolv and coverslipped as described above.

5.2.4 Imaging and quantification

All stained samples were imaged via the EVOS microscope. MATLAB was used to quantify the H&E, and Image J was used to quantify Masson's trichrome, and IHC staining. A MATLAB code was programmed to automate the quantification of the fibrous capsule of the H&E stains. The fibrous capsule from Masson's trichrome stain and macrophage expression from IHC were quantified at the hydrogel-tissue interface of both the left and right sides of the hydrogel. To quantify the fibrous capsule in the H&E and Masson's trichrome stain, a line was drawn from the edges of the fibrous capsule, and the length (in pixels) was measured. The value in units of pixels was converted to um based on the magnification of the image. To quantify the macrophage expression, the polygon selection tool in ImageJ was used to draw a small section at the interface. The pixel intensity within the section was measured to determine the macrophage expression. Sections of approximately equal area were drawn on the top and bottom of the hydrogel for each side, resulting in a total of 4 different regions in each section, and two sections per sample. Negative controls were included for each IHC experiment as a baseline for comparison.

5.2.5 Statistical analysis

Data are reported as mean ± standard deviation (SD). Statistical analysis was performed in MATLAB using one-way ANOVA with Tukey post hoc analysis on *in vitro* characterization experiments in order to determine statistical significance. A two-way ANOVA with Tukey post hoc analysis was performed on the *in vivo* histological stainings to determine statistical significance. A p-value of less than 0.05 was considered significant. Student t-test was performed to determine statistical significance between the left and right side of the hydrogel. Correlation analyses were conducted to determine any relationships between the macrophage phenotype and the fibrous capsule thickness. The Pearson's correlation coefficient was calculated at 2-tailed 95% confidence interval.

5.3. Results

5.3.1 Histological and correlation analyses

5.3.1.a H&E staining and quantification

In H&E stains, the cell nuclei were stained blue, while the cell cytoplasm was stained red or pink. The blue layer of cells deposited at the hydrogel to tissue interface was determined to be part of the fibrous capsule or the foreign body response. Therefore, each image was quantified by measuring the thickness of this outer layer surround the hydrogels.

The fibrous capsule was quantified through a multi-step imaging process in MATLAB as illustrated figure 11. Initally, the H&E images were captured via the EVOS microscope at 4x magnification and were stitched together to recreate the entire sample.

The RGB images were converted to binary based on the threshold of the pixels at the hydrogel-tissue interface. Isolated pixels were filtered to reduce the background noise. Neighboring pixels with gaps or hole were filled in order to connect the missing pixels at the interface. All background noises were then removed, and the area this interface was calculated. The perimeter of the interface was also calculated by shrinking the width to a line and determining the length of the line. To calculate the thickness of the fibrous capsule, the total area was divided by the perimeter or the length of the total sample.

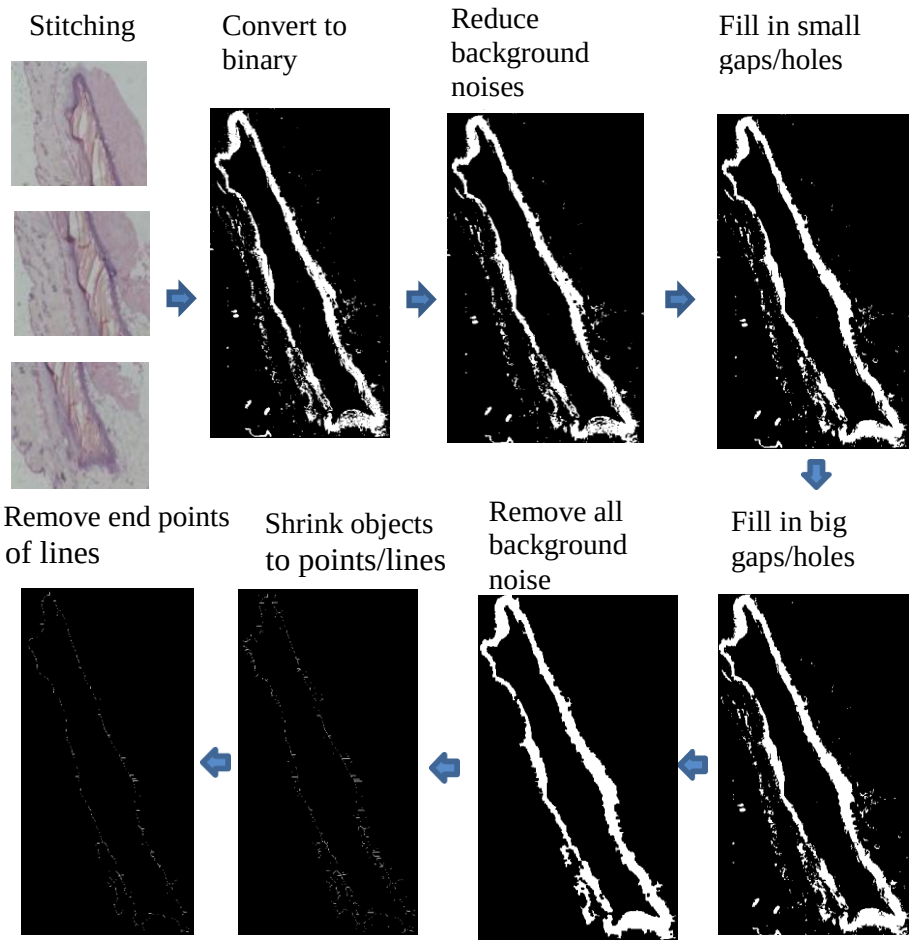

Figure 10: A MATLAB code that quantifies the fibrous capsule via image processing.

In order to verify that the output of the MATLAB code was a good representation of the actual thickness of the fibrous capsule, the pixels of a zoomed in image at 20x magnification of the fibrous capsule was manually measured in ImageJ. The MATLAB code did in fact give an accurate representation of the actual fibrous capsule as illustrated in figure 12.

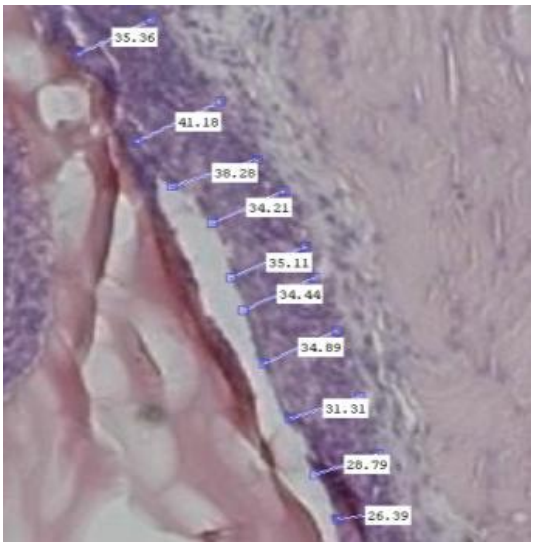

Figure 11: The thickness of the fibrous capsule was measured in ImageJ to verify the MATLAB quantification.

The thickness of the fibrous capsule was imaged and measured for each time point and crosslinking concentration (Figure 14 and 15). In general, an increase in the fibrous capsule thickness was observed with increasing crosslinking concentration and time. A two-way ANOVA analysis revealed that there was statistical significance between values at each time point, but no statistical significance between the crosslinking

concentrations. Figure 13 illustrates the general representation of the H&E images of the samples.

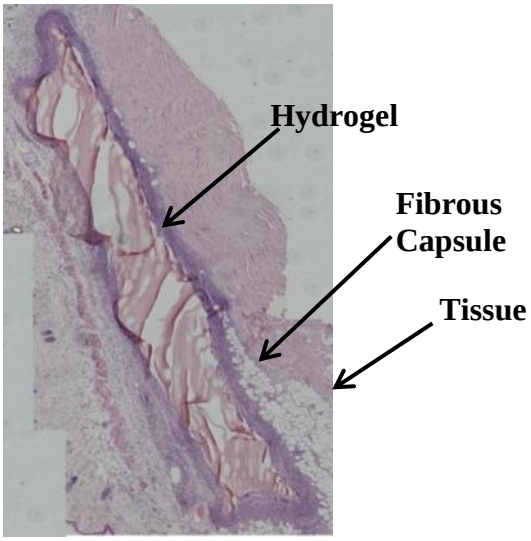

Figure 12: A labeled H&E image to illustrate the infiltration of cell surrounding the hydrogel.

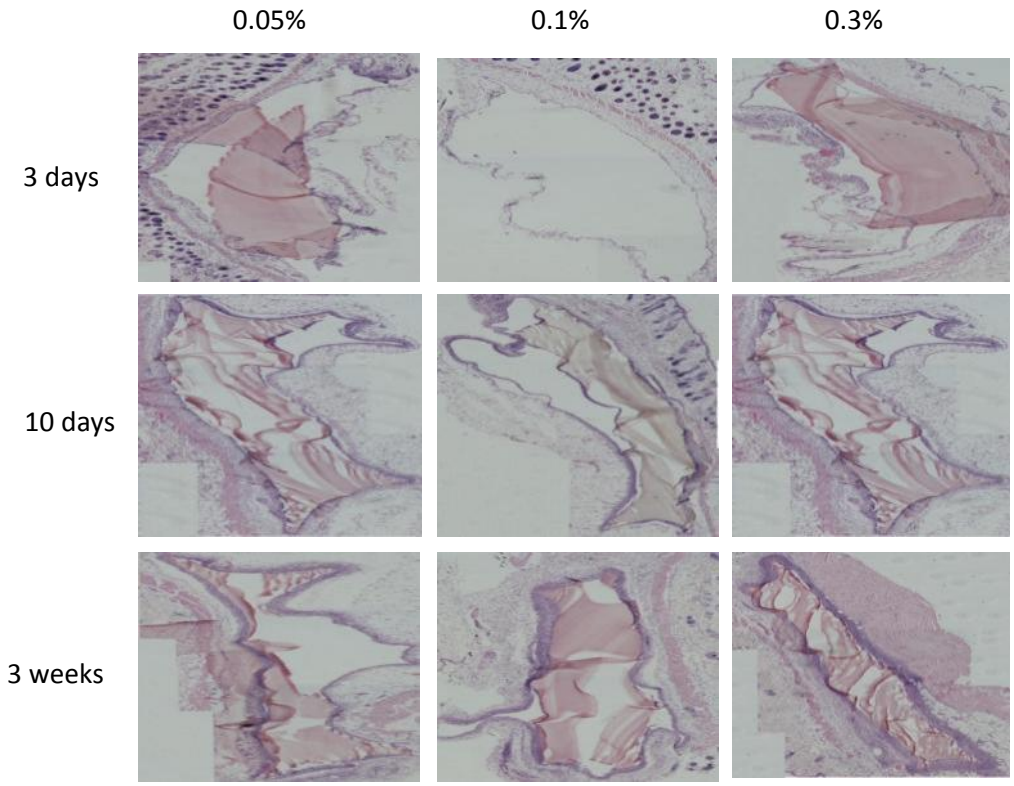

Figure 13: H&E images showing the difference in fibrous capsule of the 3 crosslinked hydrogels at the 3 time point

Table 7: The MATLAB quantification of the fibrous capsule from the H&E images

Fibrous Capsule Thickness	0.05%	0.1%	0.3%
3 days	18.2±8.27	23.9±6.69	26.6±3.00
10 days	35.9±7.85	38.2±5.53	39.8±5.88
3 weeks	45.9±2.24	46.1±5.23	51.3±13.0

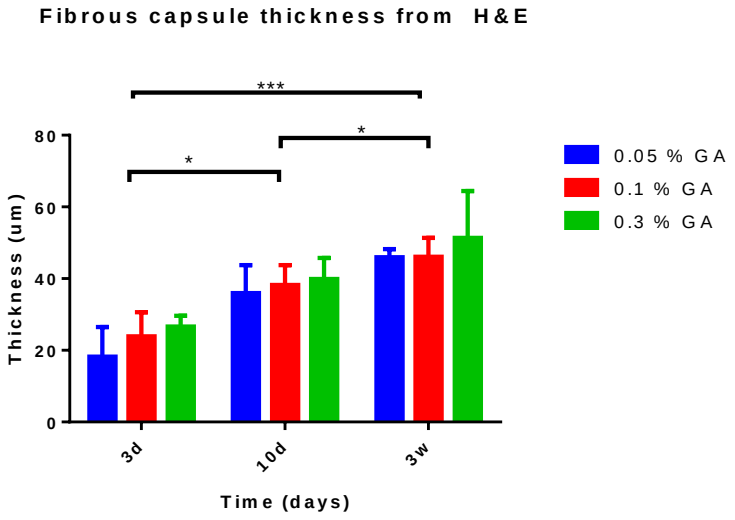

Figure 14: Graphical representation of the thickness of the fibrous capsule quantified using the MATLAB code from H&E images. * denotes p<0.05, * denotes p<0.005.**

The fibrous capsule thickness increases with time, which is consistent with the current literature in chronic wound of implanted biomaterials. However, the fibrous capsule is mainly composed of collagen, which is not quantifiable in the H&E staining. Therefore, another staining method was utilized to verify the fibrous capsule thickness from the H&E staining.

5.3.1.b Masson's trichrome stain

The Masson's trichrome is the standard staining method to quantify the fibrous capsule as it stains collagen blue and nuclei red or pink. Similar to the H&E stains, the thickness of the fibrous capsule was quantified at the hydrogel-tissue interface as illustrated in figure 16A and 16B. The fibrous capsule was quantified by imaging each

sample at 20x magnification and measuring the fibrous capsule via ImageJ. Both the cell nuclei and collagen at the site of the interface was measured as the fibrous capsule as indicated in figure 17. From the H&E stains, it was observed that there were differences on the left and right sides of the interface of the hydrogels. As a result, the fibrous capsule on both sides of the hydrogel-tissue interface was quantified to determine any physiological difference between the muscle and skin side of the implant.

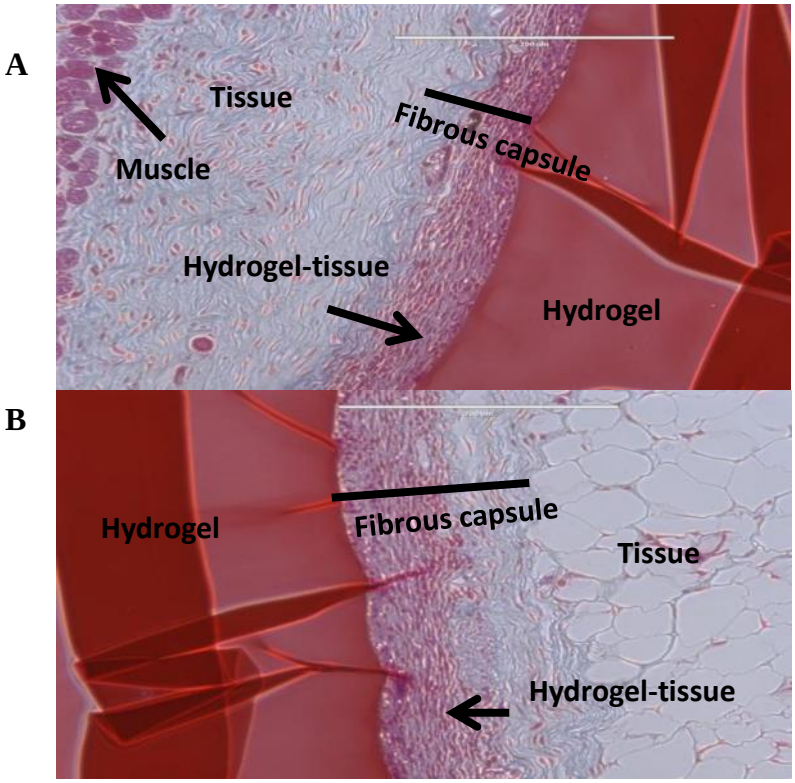

Figure 15: Labeled Masson's trichrome image to illustrate the collagen and infiltration of cells around the hydrogels

The fibrous capsule was quantified for the three crosslinked samples at each time point (Figure 20). On both sides of the hydrogel, there was no observable trend in the fibrous

capsule thickness between the three different crosslinking concentrations. Student's t-test was performed to compare the thicknesses of the left and right sides of the hydrogels. The analysis revealed no statistical significance between the two sides. Thus, the thicknesses of the two sides were averaged for further analysis. A two-way ANOVA analysis indicated that there was statistical significance as to the effect of time, but no statistical significance was observed from the crosslinking concentration. The fibrous capsule thickness was significantly thicker at the 3 week time point compared to the 3 and 10 day time points, while the 10 day time point was significantly thicker compared to the 3 day time point. The increase in the fibrous capsule thickness can be visually seen over time as illustrated in figures 16, 17, and 18.

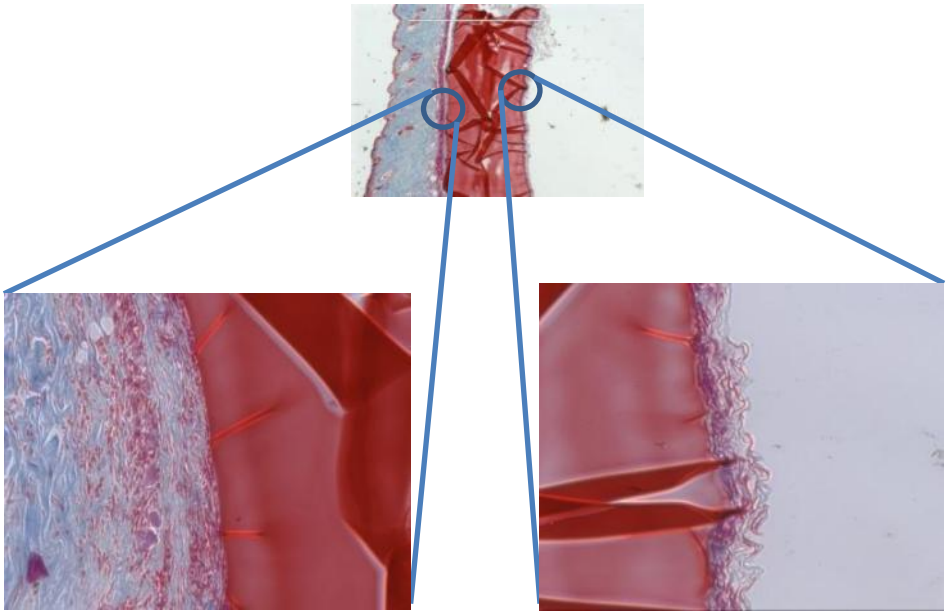

Figure 16: A 4x magnification of the Masson's trichrome stain of a 3 day 0.1% hydrogel zoomed in to a 20x magnification at both sides of the hydrogel

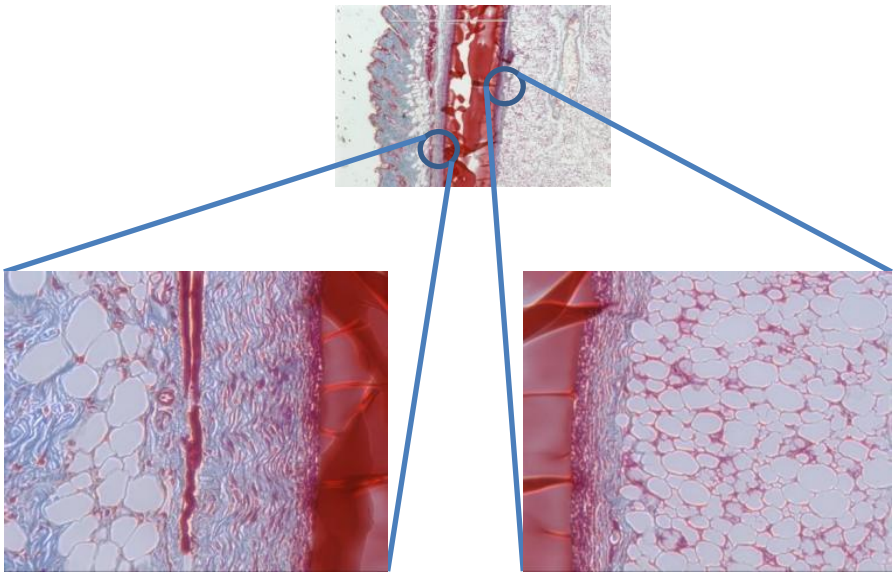

Figure 17: A 4x magnification of the Masson's trichrome stain of a 10 day 0.1% hydrogel zoomed in to a 20x magnification at both sides of the hydrogel

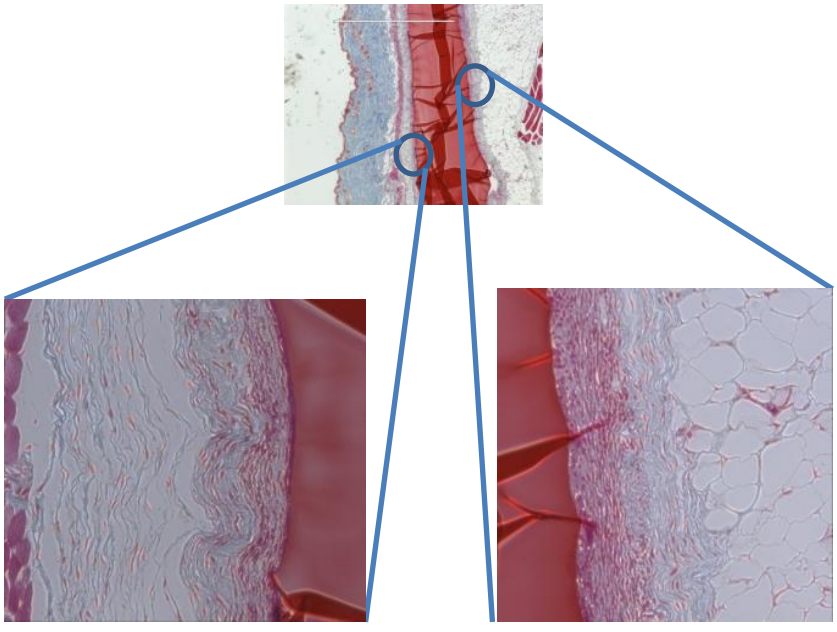

Figure 18: A 4x magnification of the Masson's trichrome stain of a 3 week 0.3% hydrogel zoomed in to a 20x magnification at both sides of the hydrogel

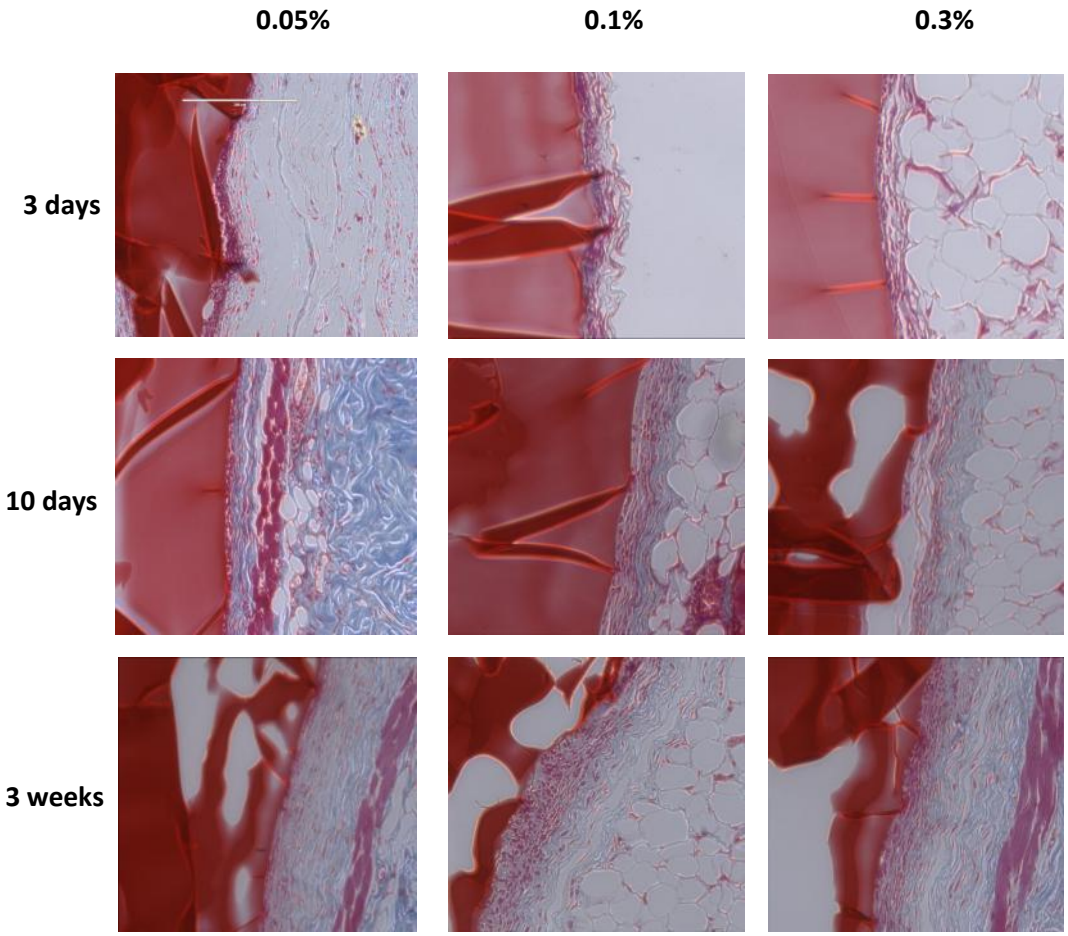

Figure 19: Masson's trichrome images at 10x magnification showing the difference in fibrous capsule of the 3 crosslinked hydrogels at the 3 time points.

Table 8: Masson's trichrome quantification of the fibrous capsule thickness on both sides of the hydrogel (units are in um)

Fibrous Capsule Thickness	3 days			10 days			3 weeks		
Mean± SD	0.05%	0.1%	0.3%	0.05%	0.1%	0.3%	0.05%	0.1%	0.3%
Left	32.1± 10.4	35.3± 11.4	30.3± 10.7	46.7± 14.3	46.7± 16.1	49.8± 7.79	96.5± 23.3	81.8± 30.3	95.3± 21.0
Right	32.5± 9.88	31.9± 10.6	29.9± 6.09	50.2± 7.96	44.8± 6.65	54.6± 13.2	84.0± 18.1	64± 5.4	82.6± 25.2
Mean	24.8± 9.71	25.9± 10.6	22.1± 8.44	34.9± 11.2	32.7± 12.2	39.2± 10.5	66.2± 20.9	50.4± 22.7	67.7± 23.1

Both the Masson's trichrome and H&E stains indicated that there was statistical significance in the thickness of the fibrous capsule between each time point, but no significance in the thickness of the fibrous capsule between the crosslinking concentrations. However, a student t-test indicated that the fibrous capsule quantified from the Masson's trichrome stain was significantly higher than the fibrous capsule quantified from the H&E stain for all samples except the sample of 0.3% at 3 day time point (Figure 21). The Masson's trichrome stain is a better quantification of the fibrous capsule because this methods stains for collagen, which makes up the fibrous capsule,

whereas H&E only stains for cell nuclei. Therefore, values obtained from Masson's trichrome were used for further analysis.

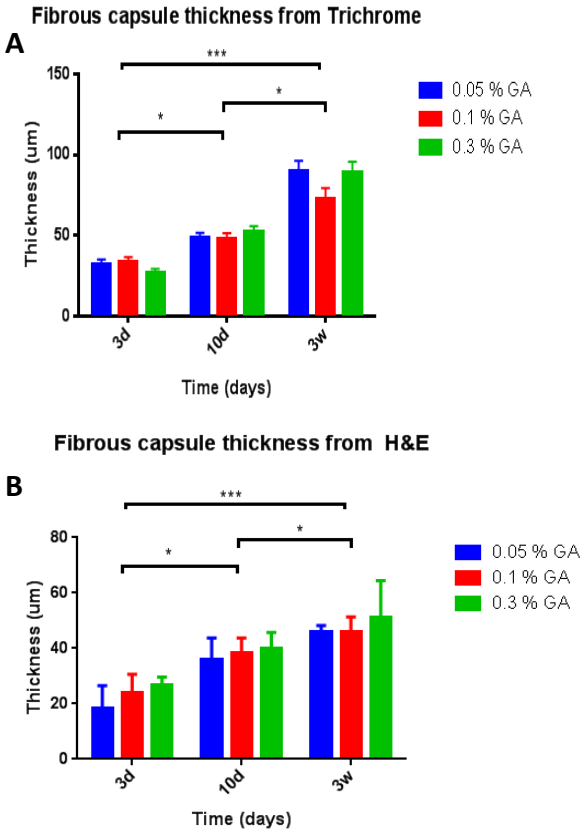

Figure 20: The comparison between the fibrous capsule thickness quantified from H&E and the fibrous capsule thickness quantified from Masson's trichrome. * denotes p<0.05, * denotes p<0.005.**

5.3.1.c Macrophage phenotyping by immunohistochemistry

IHC was performed on each sample and stained for specific surface markers to identify the M1 and M2 macrophages. The M1 macrophages were indicated by iNOS staining, while M2 macrophages were indicared by Arg1 and CD163 staining. In order to

determine real staining from background staining, negative and positive controls samples were included each time IHC experiment was performed. Sections of mouse spleen were used as the positive control. The difference in staining between the negative and positive controls is portrayed in figure 22. Samples with higher expression of macrophage markers result in dark brown stains as seen in the mouse spleen. When quantifying intensity of RGB images, darker pixels have lower values than lighter pixels. Therefore, to convert the values to values that are proportional to the darkness of the stain, and thus the intensity of macrophage marker expression, the intensity of a sample was divided by the intensity of the negative control, representing fold change over the negative control. This value is then subtracted from 1 so that darker stains have higher values.

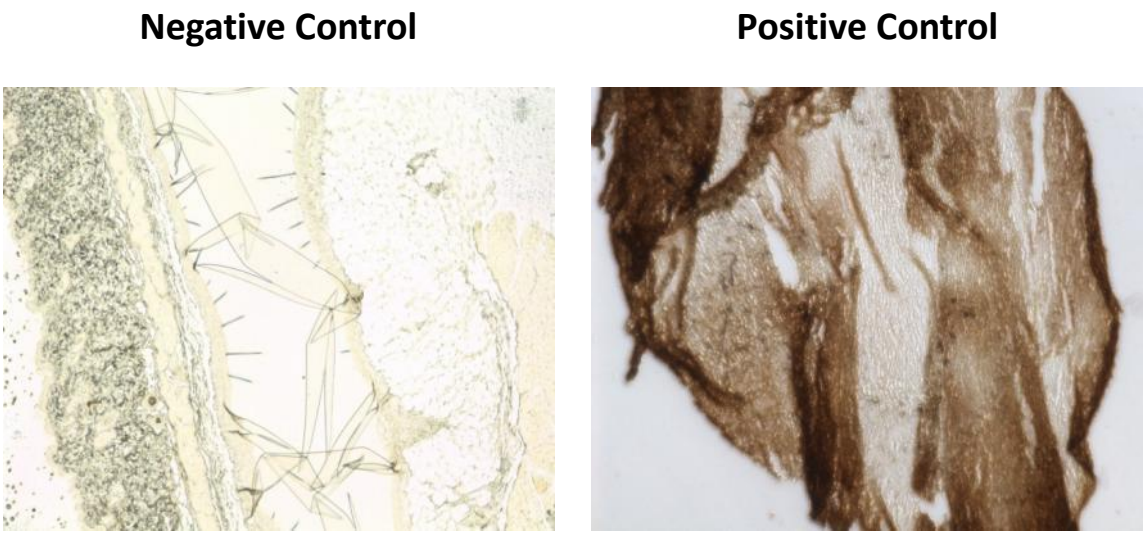

Figure 21: The negative and positive controls of an IHC stain.

The intensity of each surface marker was evaluated at four different locations, the top and bottom of the left and right sides of the hydrogel. A Student's t-test was performed to

indicate there was no statistical difference between the two sides. Thus, the expression of iNOS on both sides was averaged for further analysis to give a fair representation of the marker expression in each sample (Figure 23).

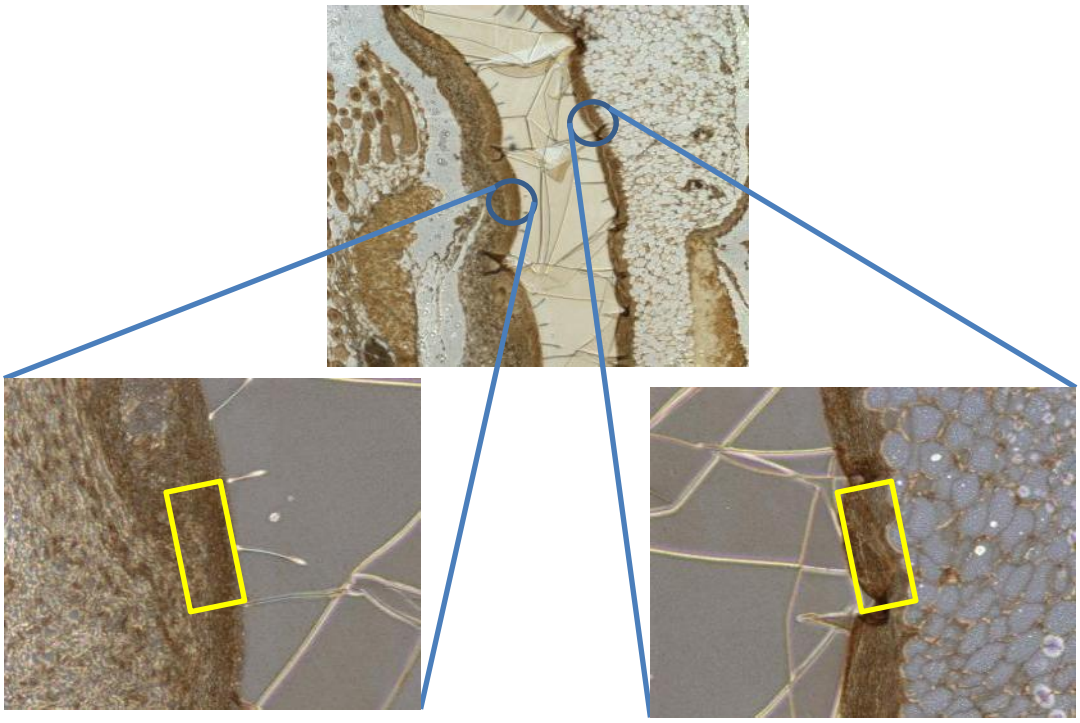

Figure 22: The intensity of the IHC staining was quantified within the yellow rectangular boxes.

Although the analysis showed that there was a slight decrease in the iNOS expression from the 3 day time point to the 3 week time point, it was not statistically significant. However, it was interesting to note that the post hoc analysis showed a significant difference in the iNOS expression of the 0.05% and 0.1% concentration, while there was no statistical significance between the 0.05% and 0.3% or between the 0.1% and 0.3% for all time points. As expected, samples at all time points resulted in high

expression of iNOS indicating an infiltration of M1 macrophages throughout the experiment (Figure 24). The data showed that there is a constant presence of the M1 macrophage indicating a chronic inflammation, which deviates from the M1 profile of normal wound healing in which the numbers of M1 macrophages subside after 5 days.

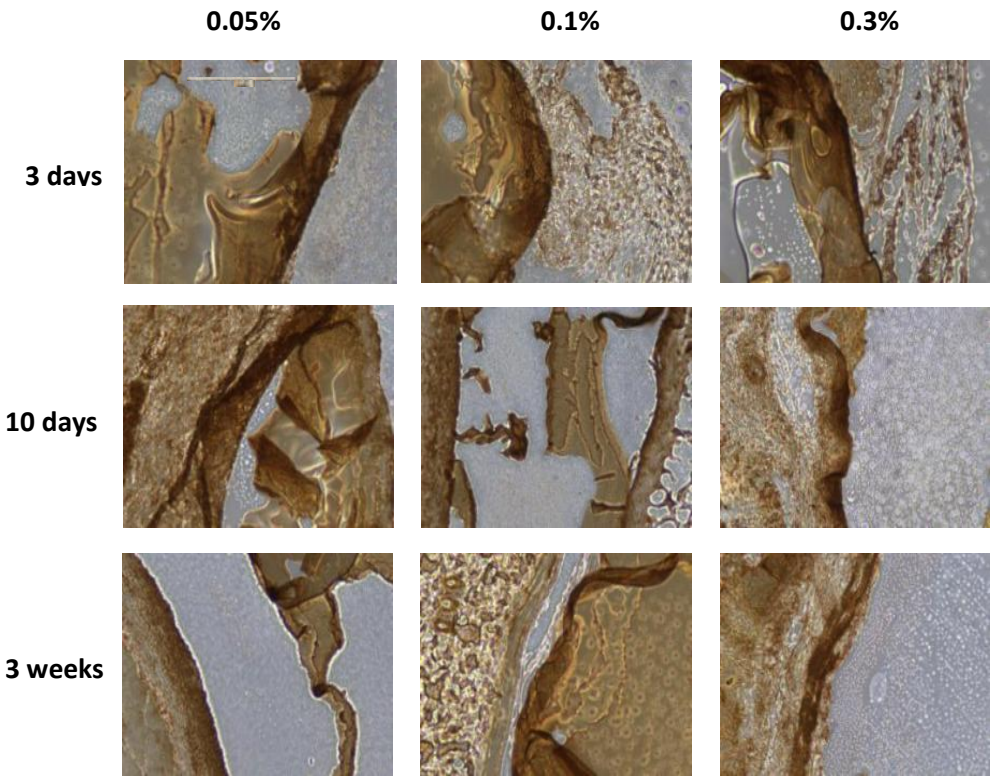

Figure 23: iNOS staining quantification at 20x magnification of the 3 crosslinked hydrogels at the 3 time points.

Similarly, the expression of both M2 markers Arg1 and CD163 was quantified on both sides (Figure 25 and 26), which were not statistically different. With the average of the both sides, a two-way ANOVA analysis was conducted to determine the effect of the crosslinking and time. For the M2 surface markers, there was no statistical difference of

the Arg1 and CD163 expression between the crosslinked hydrogels. However, there was a statistical difference in the marker expression of both markers with respect to time. The marker expressions at the 3 week time points were significantly higher than that of both the 3 day and 10 day time points. The marker expressions at the 10 day time points were significantly higher than that of the 3 day time point. It seems that the M2 macrophage profile behaves similar to that of mathematical model of normal wound healing in that the M2 macrophage slowly proliferate initially and accumulates over time. However, more time points in the *in vivo* study are needed to determine how the M2 macrophages behave after the 3 week time point in a chronic wound.

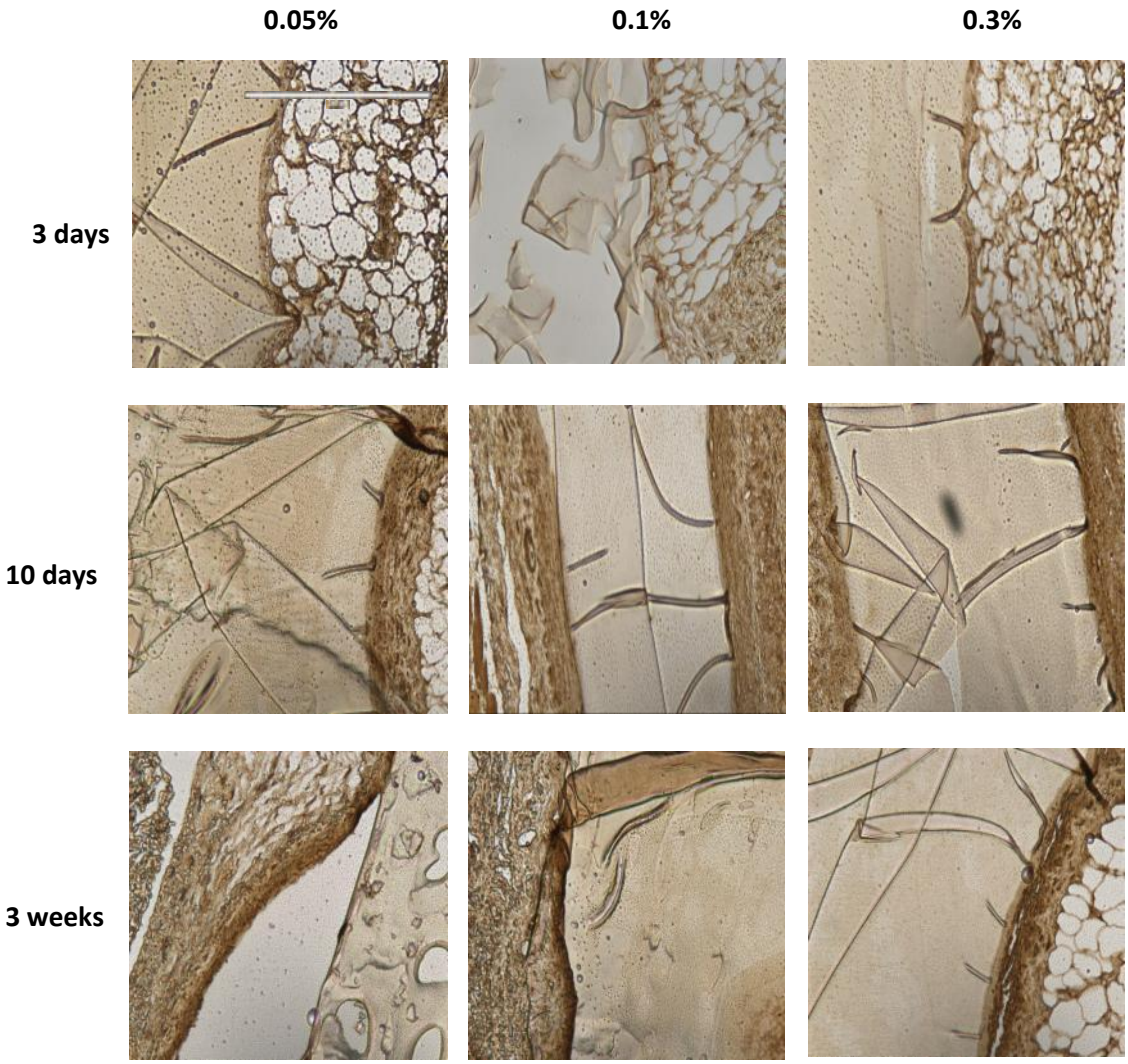

Figure 24: Arg1 staining quantification at 20x magnification of the 3 crosslinked hydrogels at the 3 time points.

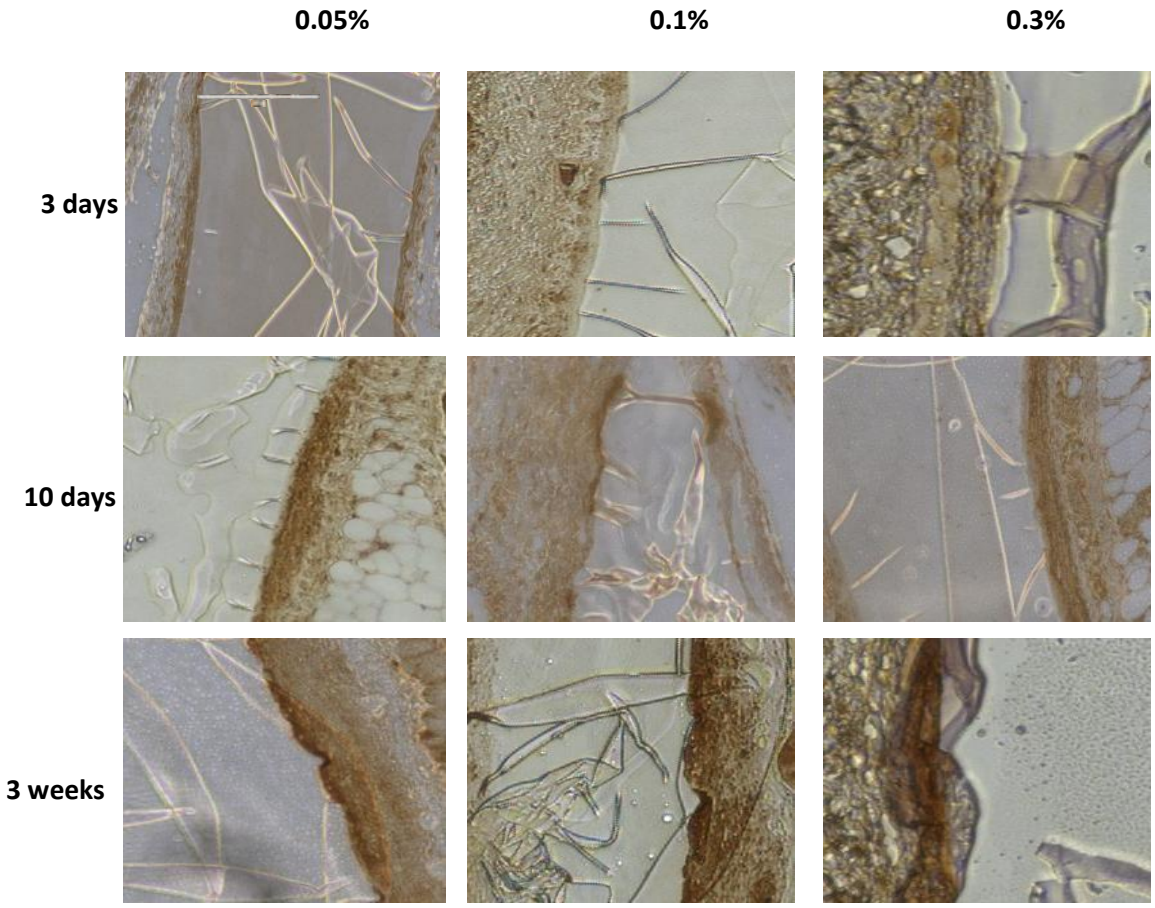

Figure 25: CD163 staining quantification at 20x magnification of the 3 crosslinked hydrogels at the 3 time points.

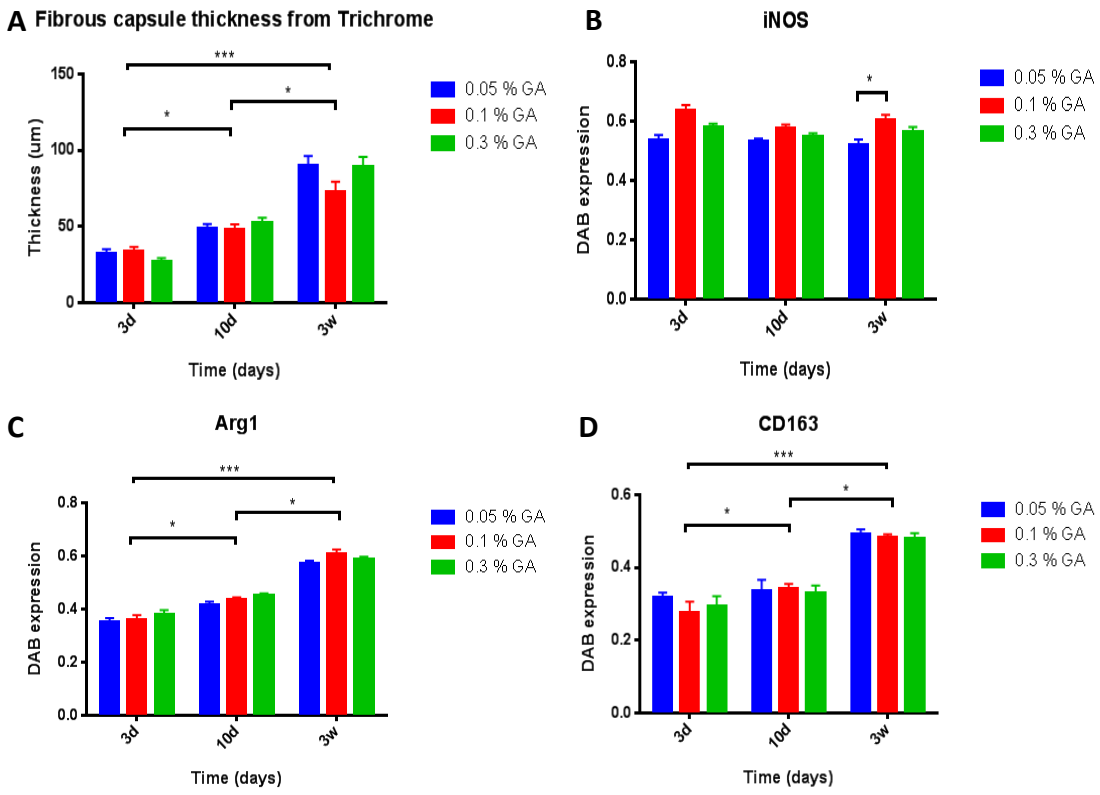

Figure 26: The quantification of the fibrous capsule thickness and the macrophage phenotype. A. Quantification of the thickness of the fibrous capsule. B. Quantification of iNOS staining. C. Quantification of Arg1 staining. D. Quantification of CD163 staining. * denotes $p<0.05$, * denotes $p<0.005$**

Table 9: **Quantification of the intensities of the three surface markers**

Intensity of Stain	3 days			10 days			3 weeks		
Mean ± SD	0.05%	0.1%	0.3%	0.05%	0.1%	0.3%	0.05%	0.1%	0.3%
iNOS	0.537 ± 0.055	0.634 ± 0.068	0.581 ± 0.032	0.531 ± 0.034	0.576 ± 0.039	0.546 ± 0.043	0.518 ± 0.069	0.604 ± 0.059	0.563 ± 0.055
Arg1	0.351 ± 0.051	0.358 ± 0.064	0.378 ± 0.061	0.415 ± 0.045	0.436 ± 0.027	0.450 ± 0.030	0.570 ± 0.041	0.607 ± 0.058	0.586 ± 0.038
CD163	0.318 ± 0.043	0.276 ± 0.103	0.294 ± 0.093	0.335 ± 0.105	0.341 ± 0.045	0.329 ± 0.073	0.493 ± 0.038	0.481 ± 0.032	0.479 ± 0.050

The ratio of M1:M2 indicated which macrophage phenotype is dominant at each time point. A ratio greater than 1 implies a dominant M1 or inflammatory phenotype, whereas, a ratio less than 1 implies a dominant M2 phenotype. Since there are two M2 markers, both iNOS:Arg1 and iNOS:CD163 ratios were calculated and averaged because both surface markers followed the same trend of increasing intensity expression over time. The M1:M2 ratio decreased over time, with the M1 phenotype initially dominating at the early time points and the M2 phenotype dominating at later time points.

Table 10: M1:M2 ratio to indicate the macrophage phenotype at each time point

M1:M2 ratio	3 days			10 days			3 weeks		
	0.05%	0.1%	0.3%	0.05%	0.1%	0.3%	0.05%	0.1%	0.3%
iNOS:Arg1	1.52	1.76	1.53	1.27	1.32	1.21	0.908	0.996	0.960
iNOS:CD163	1.69	2.29	1.97	1.58	1.68	1.65	1.05	1.25	1.17
Mean±SD	1.60± 0.113	2.03± 0.374	1.75± 0.311	1.43± 0.214	1.50± 0.258	1.43± 0.315	0.979± 0.100	1.12± 0.183	1.06± 0.152

The IHC staining revealed that the macrophage profile of a chronic wound due to biomaterial implantation deviated from that of normal wound healing. Unlike normal wound healing, the M1 macrophages surrounded the hydrogels throughout the 3 week study. The quantification of the M1 macrophages showed a relatively high expression of iNOS at all time points, indicating chronic inflammation. However, the M2 macrophage profile followed a similar course of behavior compared to that of normal wound healing. Initially, there was a low expression of Arg1 at the early time point. The expression of Arg1 progressed with time. Similar to normal wound healing, the M2 macrophages slowly surrounded the hydrogel over time and eventually accumulated. The results seem consistent with the idea of a chronic wound in that a prolonged inflammatory response exists due of the presence of the implanted hydrogel.

5.3.2 Correlation Analyses

Correlation analyses were performed to determine any relationships between the macrophage phenotype and the fibrous capsule thickness (Figure 28). The correlation analysis revealed a strong negative relationship between the M1:M2 ratio and the

thickness of the fibrous capsule with a Pearson's correlation coefficient of -0.836. This suggests that a lower M1:M2 ratio or a M2 dominant phenotype correlates with a thicker fibrous capsule. The correlation analysis also indicated a very weak relationship between iNOS and the thickness of the fibrous capsule with a Pearson correlation coefficient of -0.295. In contrast, there was a strong positive relationship between the M2 surface markers, Arg1 and CD163, and the thickness of the fibrous capsule with a Pearson correlation coefficient of 0.948 and 0.959, respectively. These correlation analyses suggest that the M2 macrophages, not the M1 macrophages, are responsible for the increase in the fibrous capsule thickness.

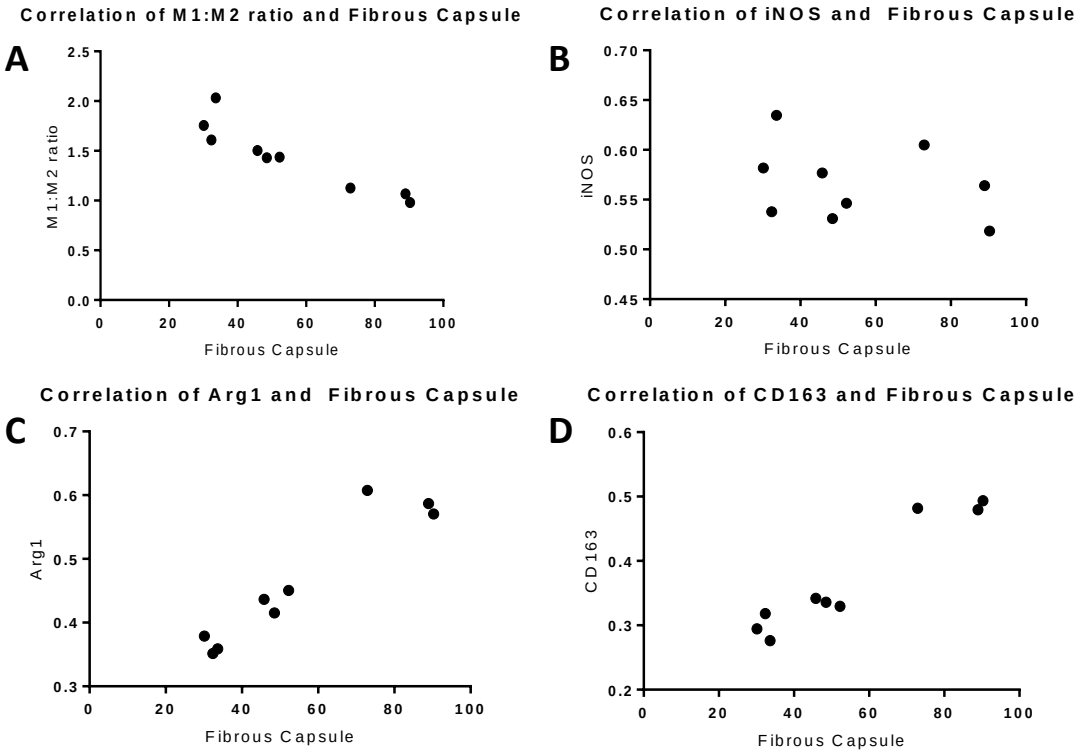

Figure 27: The correlation analyses to the fibrous capsule thickness. A. The correlation between the M1:M2 ratio and the fibrous capsule. B. The correlation between the iNOS intensity and the fibrous capsule. C. The correlation between the Arg1 intensity and the fibrous capsule. D. The correlation between the CD163 intensity and the fibrous capsule.

Table 11: Correlation coefficients of the M1:M2 ratio and iNOS, Arg1, and CD163 to the fibrous capsule thickness

Correlation to the fibrous capsule thickness	Correlation Coefficient, r
M1:M2 ratio	-0.922
iNOS	-0.295
Arg1	0.948
CD163	0.959

Chapter 6: Discussion

Many models have attempted to explain the behavior of macrophages in normal wound healing. However, these models do not include accurate macrophage biology experiments, either *in vitro* or *in vivo*, to support or justify their parameters resulting in physiologically irrelevant or incomplete results [62, 63]. The mathematical model described in this work has several advantages over the existing models because this model takes into account accurate macrophage profile behavior in normal wound healing. In addition, the parameter values in this model are based on *in vitro* experiments making this model more physiologically relevant to the foreign body response *in vivo*. Other studies chose parameter values that would best fit the model, which would then require uncertainty and sensitivity analyses. In contrast, this model does not require these analyses because the parameters were based on experimental data from macrophages cultured in controlled environments. This model was able to model the M0, M1, and M2

macrophage population during a period of 30 days. The macrophage profiles were consistent with the current macrophage biology of normal wound healing similar to the studies by Troidl et al. [70, 71]. Likewise, these studies showed a M1 dominant phenotype 3-5 days post-injury and an M2 dominant phenotype afterwards.

Some limitations to this mathematical model include the fact that it only models macrophages in wound healing and does not taking into account of other important cell types such as fibroblasts. In addition, the polarization and transition rate constants were assumed to be the same throughout the wound healing process, which may not be the case at each time point or stages of wound healing. Furthermore, the migration of M0 rate to the wound site was based on literature and is not as accurate as performing experiments to obtain the value. The macrophages also do not return back to pre-injury levels because the macrophage profiles reached an equilibrium in the system. Because the newly arriving M0 macrophage rate is incorporated, it offsets the death rates, consequently leading to a steady state over time in the system. Most importantly, the *in vitro* experiment was done three times with a replica of 1. For each experiment, each of the macrophage population followed a similar trend indicating a good representation of the macrophage profiles *in vitro*. However, the time points were only taken at an interval of 1 day. As a result, the rate constants were calculated from the slope of its respective time points, which does not take into consideration of the macrophage profiles in between the time points at each day. A possible solution to obtain a better representation of the macrophage profile in between each time points is to implement a curve fitting model to the data points. Consequently, the *in vitro* experiment should be repeated to include more time points at a smaller intervals in order to obtain the M0 migrate rate, accurately

describe the macrophage dynamics, and to confirm the results from this study. And because of the limited data available from the *in vitro* experiments, the polarization rates were only approximations of the actual rates. More time points are needed throughout the study to more accurately determine the values of each parameter. Although there are some drawbacks to the mathematical model, it does describe the macrophage profile in wounds reasonably well.

To represent a chronic wound in the mathematical model, the transition from M1 to M2 was deleted from the system of equations (Figure 29), which has been suggested as the mechanism of wound healing impairment in chronic wounds [73]. In the "chronic wound" model, the M1 macrophages dominate throughout the experiment representing a chronic inflammation, which was also observed in the IHC staining of the implanted hydrogels as well. Even though there was a greater amount of M1 macrophages than the M2 throughout the 30 days, the model describes the M1 macrophages decreasing after the initial peak at day 3, which was not observed in the IHC staining of the *in vivo* experiment. The IHC staining showed a constant infiltration and amount of M1 macrophages throughout the 3 week time frame, which was not predicted from the "chronic wound" model. Furthermore, the M2 population in this model decreases from the original model. This was also not observed in the IHC staining in the *in vivo* biomaterial implantation study, as there were increasing M2 macrophages from the day 3 to week 3. This indicates that either this "chronic wound" model does not accurately represent macrophage response to biomaterial implantation, or biomaterial implantation affects macrophage behavior in other ways besides the M1 to M2 transition.

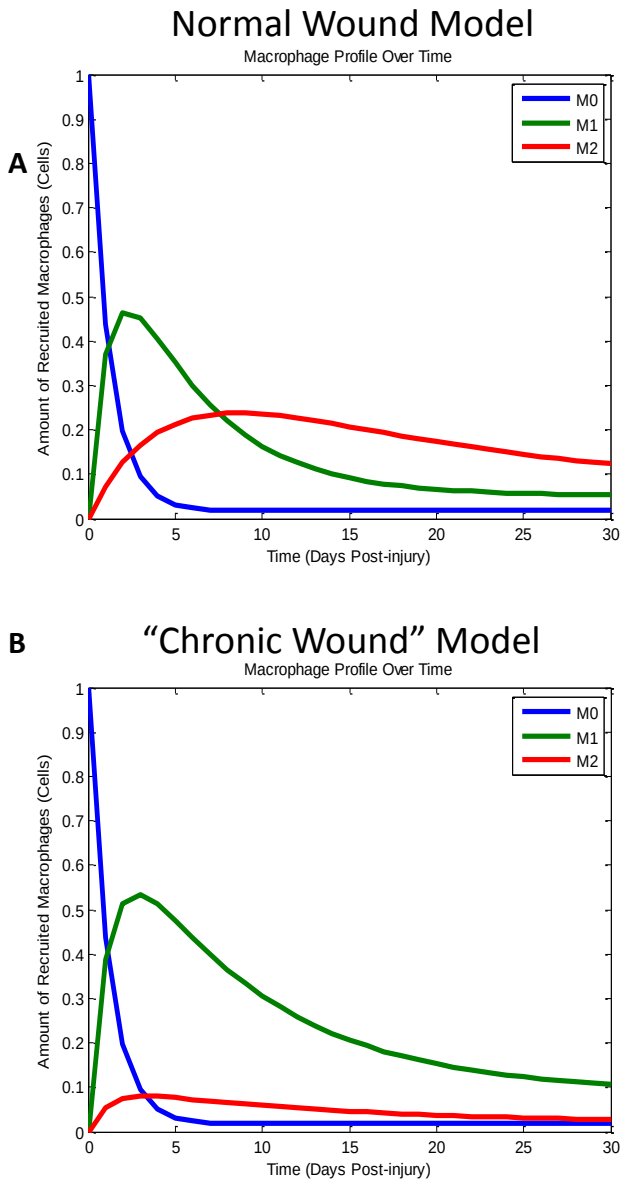

Figure 28: A comparison of a chronic wound via deletion of the M1-to-M2 term to the normal wound healing model

The roles of the different macrophage phenotypes in the FBR are still controversial and not well understood. The M1 phenotype that is responsible for the inflammatory response has been associated with formation of the fibrous capsule [47,

51], while the M2 phenotype has been often associated with wound healing and tissue remodeling [49, 50]. However, the results from the present study and others [52] have showed that the M2 phenotype may be more responsible for the formation of the fibrous capsule than the M1 phenotype. Although the M1 phenotype contributes to the inflammatory response and the FBR, the M2 phenotype is known to secrete cytokines such as PDGF-BB and TGFB that directly promote recruitment of fibroblast, which may lead to the formation of fibrotic tissue and eventually the fibrous capsule [5, 52, 74]. To gain a better understanding of the FBR, *in vivo* animal studies were conducted in order to compare the macrophage profile of a chronic wound of an implanted biomaterial to that of normal wound healing. Gelatin hydrogels crosslinked with GA were chosen as a model biomaterial to examine the roles of macrophage phenotypes in the formation of the fibrous capsule and the FBR. The characterization of the hydrogels showed that the each of the crosslinked hydrogels were significantly different form each other in terms of mechanical stiffness, swelling, degradation, and crosslinking density.

The IHC staining and quantification of iNOS, Arg1, and CD163 surface markers also showed similar results, which revealed that crosslinking had no effect on the cellular infiltration of M1 and M2 macrophages. Interestingly, these properties did not result in differences in the FBR or the thickness of the fibrous capsule. The crosslinking of the hydrogels increases the mechanical stiffness, which has been shown to increase macrophage activation thereby inducing a more severe FBR [75]. On the other hand, some studies have showed that chemical crosslinking does not induce any detrimental effects *in vivo* in terms of the FBR and biocompatibility [65]. More importantly, studies have shown that GA crosslinking is not cytotoxic to fibroblasts and even promote

vascularization when implanted subcutaneously in rodents [67]. Hydrogels crosslinked with GA have shown to be non-cytotoxic when washed at least two times after the crosslinking process [67]. The gelatin hydrogels that were crosslinked at a higher GA concentration resulted in higher stiffness, but no effect was observed in the FBR or the thickness of the fibrous capsule. In addition, the initial sterilization of the crosslinked gelatin hydrogels under UV light for 2 hours prior to implantation could have further crosslinked all the hydrogels. It is speculated that the UV light may have contributed to further crosslinking the hydrogels increasing the mechanical properties of the hydrogels, which would account for the statistically similar results of the *in vivo* study. However, further experiments are required to support this theory.

The M1 macrophages were strongly stained for iNOS at all time points indicating an infiltration of M1 macrophages throughout the study. The constant presences of the hydrogels in the body cause the macrophages to become frustrated as they cannot phagocytose or degrade the foreign material causing chronic inflammation in the wound. Both the Arg1 and CD163 quantification revealed that there was weak staining at 3 day post-implantation, mild staining at 10 day post-implantation, and strong staining at 3 week post-implantation. Although this may seem to follow the behavior of M2 macrophage profile in normal wound healing, more time points are needed to determine the dynamics of the M2 macrophages between each of these time points and after 3 weeks. From these results, a chronic wound from implantation deviates from normal wound healing in that the M1 macrophages are constantly present and infiltrating the foreign material.

At 3 days post-implantation, the amount of M1 macrophages is almost twice the amount of the M2 macrophages. At 3 week post-implantation, there is almost an equal amount of M1 and M2 macrophages as evidence by a ratio of approximately 1. Although the correlation analyses show that the M1:M2 ratio was strongly negatively correlated with the fibrous capsule thickness, the M1:M2 ratio also indicated that M1 phenotype was dominant throughout the study indicating that the M1 also contributes to the fibrous capsule. Furthermore, the correlation analyses of the expressions of Arg1 and CD163 showed a strong positive relationship with the fibrous capsule thickness. However, the M1 phenotype could be the initiating factor that causes the formation of the fibrous capsule because the fibrous capsule was already formed at 3 days post-implantation which coincides with a dominant M1 phenotype, and because M1 macrophages transition into M2 macrophages. The M2 phenotype would further increase the fibrous capsule by secreting PDGFBB and TGFB [74]. However, more studies are needed to elucidate the controversies surrounding the macrophage phenotypes and FBR and the formation of the fibrous.

Future studies of this current work include incorporating more time points and the effects of different crosslinking density and degradation rate of the biomaterials in the *in vivo* study to gain a more thorough understanding of the inflammatory response to biomaterial implantation. In addition, the mathematical model can be applied to other conditions or situations by manipulating the variables and parameters based on *in vitro* or *in vivo* experiments. Furthermore, the model can be made more sophisticated by modeling different cell types including fibroblasts and neutrophils, which are also

important in wound healing. Other model biomaterials could also be used to determine whether the macrophage profiles follow the same trends as the present study.

Chapter 7: Conclusions

A mathematical model was developed, which successfully modeled the M0, M1, and M2 macrophage population in normal wound healing based on *in vitro* experiments. The model was able to accurately represent the macrophage dynamics in normal wound healing. *In vivo* studies were also done to assess the FBR of a chronic wound by implanting crosslinked gelatin hydrogels in mice subcutaneously. Hydrogels were crosslinked to different extents to determine any difference in the FBR to the mechanical stiffness and degradation rate of the hydrogels. After three different time points chosen to fall within the stages of the initial inflammatory response, the transition between the stages of wound healing, and a pro-healing stage, the hydrogels were explanted for fixed for further analyses. Histology including H&E, Masson's trichrome, and IHC staining was performed on each sample post-implantation and determined that there was a chronic presence of M1 macrophages throughout the study, deviating from normal wound healing. The M2 macrophages were found to contribute to the increase in the fibrous capsule thickness. The modulation of the macrophage profile in a chronic wound could potentially reduce the FBR and the formation of the fibrous capsule.

Chapter 8: List of References

[1] D. M. Higgins, R. J. Basaraba, A. C. Hohnbaum, E. J. Lee, D. W. Grainger, and M. Gonzalez-Juarrero, "Localized immunosuppressive environment in the foreign body response to implanted biomaterials," *Am J Pathol,* vol. 175, pp. 161-70, Jul 2009.

[2] D. Schmidt, H. Waldeck, and W. Kao, "Protein Adsorption to Biomaterials," in *Biological Interactions on Materials Surfaces*, D. A. Puleo and R. Bizios, Eds., ed: Springer US, 2009, pp. 1-18.

[3] S. Verheye, C. P. Markou, M. Y. Salame, B. Wan, S. B. King, 3rd, K. A. Robinson, *et al.*, "Reduced thrombus formation by hyaluronic acid coating of endovascular devices," *Arterioscler Thromb Vasc Biol,* vol. 20, pp. 1168-72, Apr 2000.

[4] C. S. Chamberlain, E. M. Leiferman, K. E. Frisch, S. E. Duenwald-Kuehl, S. L. Brickson, W. L. Murphy, *et al.*, "Interleukin-1 receptor antagonist modulates inflammation and scarring after ligament injury," *Connect Tissue Res*, vol. 55, pp. 177-86, Jun 2014.

[5] K. L. Spiller, R. R. Anfang, K. J. Spiller, J. Ng, K. R. Nakazawa, J. W. Daulton, *et al.*, "The role of macrophage phenotype in vascularization of tissue engineering scaffolds," *Biomaterials,* vol. 35, pp. 4477-88, May 2014.

[6] D. W. Baker, J. Zhou, Y. T. Tsai, K. M. Patty, H. Weng, E. N. Tang, *et al.*, "Development of optical probes for in vivo imaging of polarized macrophages during foreign body reactions," *Acta Biomater,* vol. 10, pp. 2945-55, Jul 2014.

[7] D. Lickorish, J. Chan, J. Song, and J. E. Davies, "An in-vivo model to interrogate the transition from acute to chronic inflammation," *Eur Cell Mater,* vol. 8, pp. 12-9; discussion 20, 2004.

[8] J. Yang, B. Jao, A. K. McNally, and J. M. Anderson, "In vivo quantitative and qualitative assessment of foreign body giant cell formation on biomaterials in mice deficient in natural killer lymphocyte subsets, mast cells, or the interleukin-4 receptoralpha and in severe combined immunodeficient mice," *J Biomed Mater Res A,* vol. 102, pp. 2017-23, Jun 2014.

[9] D. Bakker, C. A. van Blitterswijk, S. C. Hesseling, and J. J. Grote, "Effect of implantation site on phagocyte/polymer interaction and fibrous capsule formation," *Biomaterials*, vol. 9, pp. 14-23, Jan 1988.

[10] B. D. Ratner, "Reducing capsular thickness and enhancing angiogenesis around implant drug release systems," *J Control Release*, vol. 78, pp. 211-8, Jan 17 2002.

[11] J. M. Anderson, H. Niven, J. Pelagalli, L. S. Olanoff, and R. D. Jones, "The role of the fibrous capsule in the function of implanted drug-polymer sustained release systems," *J Biomed Mater Res*, vol. 15, pp. 889-902, Nov 1981.

[12] U. Klueh, J. T. Frailey, Y. Qiao, O. Antar, and D. L. Kreutzer, "Cell based metabolic barriers to glucose diffusion: macrophages and continuous glucose monitoring," *Biomaterials*, vol. 35, pp. 3145-53, Mar 2014.

[13] U. Klueh, Y. Qiao, J. T. Frailey, and D. L. Kreutzer, "Impact of macrophage deficiency and depletion on continuous glucose monitoring in vivo," *Biomaterials*, vol. 35, pp. 1789-96, Feb 2014.

[14] M. Frost and M. E. Meyerhoff, "In vivo chemical sensors: tackling biocompatibility," *Anal Chem*, vol. 78, pp. 7370-7, Nov 1 2006.

[15] P. Moshayedi, G. Ng, J. C. Kwok, G. S. Yeo, C. E. Bryant, J. W. Fawcett, *et al.*, "The relationship between glial cell mechanosensitivity and foreign body reactions in the central nervous system," *Biomaterials*, vol. 35, pp. 3919-25, Apr 2014.

[16] R. Biran, D. C. Martin, and P. A. Tresco, "Neuronal cell loss accompanies the brain tissue response to chronically implanted silicon microelectrode arrays," *Exp Neurol*, vol. 195, pp. 115-26, Sep 2005.

[17] R. F. Padera and C. K. Colton, "Time course of membrane microarchitecture-driven neovascularization," *Biomaterials*, vol. 17, pp. 277-84, Feb 1996.

[18] T. Maki, I. Otsu, J. J. O'Neil, K. Dunleavy, C. J. Mullon, B. A. Solomon, *et al.*, "Treatment of diabetes by xenogeneic islets without immunosuppression. Use of a vascularized bioartificial pancreas," *Diabetes*, vol. 45, pp. 342-7, Mar 1996.

[19] H. Shin, P. Quinten Ruhe, A. G. Mikos, and J. A. Jansen, "In vivo bone and soft tissue response to injectable, biodegradable oligo(poly(ethylene glycol) fumarate) hydrogels," *Biomaterials,* vol. 24, pp. 3201-11, Aug 2003.

[20] L. R. Madden, D. J. Mortisen, E. M. Sussman, S. K. Dupras, J. A. Fugate, J. L. Cuy, *et al.*, "Proangiogenic scaffolds as functional templates for cardiac tissue engineering," *Proc Natl Acad Sci U S A,* vol. 107, pp. 15211-6, Aug 24 2010.

[21] L. Zhang, Z. Cao, T. Bai, L. Carr, J. R. Ella-Menye, C. Irvin, *et al.*, "Zwitterionic hydrogels implanted in mice resist the foreign-body reaction," *Nat Biotechnol,* vol. 31, pp. 553-6, Jun 2013.

[22] W. B. Tsai, J. M. Grunkemeier, and T. A. Horbett, "Human plasma fibrinogen adsorption and platelet adhesion to polystyrene," *J Biomed Mater Res,* vol. 44, pp. 130-9, Feb 1999.

[23] N. Wisniewski and M. Reichert, "Methods for reducing biosensor membrane biofouling," *Colloids Surf B Biointerfaces,* vol. 18, pp. 197-219, Oct 1 2000.

[24] C. A. Quinn, R. E. Connor, and A. Heller, "Biocompatible, glucose-permeable hydrogel for in situ coating of implantable biosensors," *Biomaterials,* vol. 18, pp. 1665-70, Dec 1997.

[25] H. Wang, G. Yue, C. Dong, F. Wu, J. Wei, Y. Yang, *et al.*, "Carboxybetaine methacrylate-modified nylon surface for circulating tumor cell capture," *ACS Appl Mater Interfaces,* vol. 6, pp. 4550-9, Mar 26 2014.

[26] M. C. Schulz, P. Korn, B. Stadlinger, U. Range, S. Moller, J. Becher, *et al.*, "Coating with artificial matrices from collagen and sulfated hyaluronan influences the osseointegration of dental implants," *J Mater Sci Mater Med,* vol. 25, pp. 247-58, Jan 2014.

[27] S. Rammelt, T. Illert, S. Bierbaum, D. Scharnweber, H. Zwipp, and W. Schneiders, "Coating of titanium implants with collagen, RGD peptide and chondroitin sulfate," *Biomaterials,* vol. 27, pp. 5561-71, Nov 2006.

[28] W. K. Ward, M. J. Quinn, M. D. Wood, K. L. Tiekotter, S. Pidikiti, and J. A. Gallagher, "Vascularizing the tissue surrounding a model biosensor: how

localized is the effect of a subcutaneous infusion of vascular endothelial growth factor (VEGF)?," *Biosens Bioelectron,* vol. 19, pp. 155-63, Nov 30 2003.

[29] R. Gifford, M. M. Batchelor, Y. Lee, G. Gokulrangan, M. E. Meyerhoff, and G. S. Wilson, "Mediation of in vivo glucose sensor inflammatory response via nitric oxide release," *J Biomed Mater Res A,* vol. 75, pp. 755-66, Dec 15 2005.

[30] S. D. Patil, F. Papadimitrakopoulos, and D. J. Burgess, "Dexamethasone-loaded poly(lactic-co-glycolic) acid microspheres/poly(vinyl alcohol) hydrogel composite coatings for inflammation control," *Diabetes Technol Ther,* vol. 6, pp. 887-97, Dec 2004.

[31] H. Cao, K. McHugh, S. Y. Chew, and J. M. Anderson, "The topographical effect of electrospun nanofibrous scaffolds on the in vivo and in vitro foreign body reaction," *J Biomed Mater Res A,* vol. 93, pp. 1151-9, Jun 1 2010.

[32] H. E. Koschwanez, F. Y. Yap, B. Klitzman, and W. M. Reichert, "In vitro and in vivo characterization of porous poly-L-lactic acid coatings for subcutaneously implanted glucose sensors," *J Biomed Mater Res A,* vol. 87, pp. 792-807, Dec 1 2008.

[33] P. C. Bota, A. M. Collie, P. Puolakkainen, R. B. Vernon, E. H. Sage, B. D. Ratner, *et al.,* "Biomaterial topography alters healing in vivo and monocyte/macrophage activation in vitro," *J Biomed Mater Res A,* vol. 95, pp. 649-57, Nov 2010.

[34] P. Verhamme and M. F. Hoylaerts, "Hemostasis and inflammation: two of a kind?," *Thromb J,* vol. 7, p. 15, 2009.

[35] G. Hubner, M. Brauchle, H. Smola, M. Madlener, R. Fassler, and S. Werner, "Differential regulation of pro-inflammatory cytokines during wound healing in normal and glucocorticoid-treated mice," *Cytokine,* vol. 8, pp. 548-56, Jul 1996.

[36] E. Song, N. Ouyang, M. Horbelt, B. Antus, M. Wang, and M. S. Exton, "Influence of alternatively and classically activated macrophages on fibrogenic activities of human fibroblasts," *Cell Immunol,* vol. 204, pp. 19-28, Aug 25 2000.

[37] S. J. Jenkins, D. Ruckerl, P. C. Cook, L. H. Jones, F. D. Finkelman, N. van Rooijen, *et al.*, "Local macrophage proliferation, rather than recruitment from the blood, is a signature of TH2 inflammation," *Science*, vol. 332, pp. 1284-8, Jun 10 2011.

[38] G. J. Bellingan, H. Caldwell, S. E. Howie, I. Dransfield, and C. Haslett, "In vivo fate of the inflammatory macrophage during the resolution of inflammation: inflammatory macrophages do not die locally, but emigrate to the draining lymph nodes," *J Immunol*, vol. 157, pp. 2577-85, Sep 15 1996.

[39] K. A. Kigerl, J. C. Gensel, D. P. Ankeny, J. K. Alexander, D. J. Donnelly, and P. G. Popovich, "Identification of two distinct macrophage subsets with divergent effects causing either neurotoxicity or regeneration in the injured mouse spinal cord," *J Neurosci*, vol. 29, pp. 13435-44, Oct 28 2009.

[40] M. L. Novak, E. M. Weinheimer-Haus, and T. J. Koh, "Macrophage activation and skeletal muscle healing following traumatic injury," *J Pathol*, vol. 232, pp. 344-55, Feb 2014.

[41] S. Willenborg, T. Lucas, G. van Loo, J. A. Knipper, T. Krieg, I. Haase, *et al.*, "CCR2 recruits an inflammatory macrophage subpopulation critical for angiogenesis in tissue repair," *Blood*, vol. 120, pp. 613-25, Jul 19 2012.

[42] L. Arnold, A. Henry, F. Poron, Y. Baba-Amer, N. van Rooijen, A. Plonquet, *et al.*, "Inflammatory monocytes recruited after skeletal muscle injury switch into antiinflammatory macrophages to support myogenesis," *J Exp Med*, vol. 204, pp. 1057-69, May 14 2007.

[43] S. J. Bullers, S. C. Baker, E. Ingham, and J. Southgate, "The Human Tissue-Biomaterial Interface: A Role for PPARgamma-Dependent Glucocorticoid Receptor Activation in Regulating the CD163 M2 Macrophage Phenotype," *Tissue Eng Part A*, May 20 2014.

[44] T. Ito, T. Kaneko, Y. Yamanaka, Y. Shigetani, K. Yoshiba, and T. Okiji, "M2 macrophages participate in the biological tissue healing reaction to mineral trioxide aggregate," *J Endod*, vol. 40, pp. 379-83, Mar 2014.

[45] S. A. Villalta, H. X. Nguyen, B. Deng, T. Gotoh, and J. G. Tidball, "Shifts in macrophage phenotypes and macrophage competition for arginine metabolism

affect the severity of muscle pathology in muscular dystrophy," *Hum Mol Genet,* vol. 18, pp. 482-96, Feb 1 2009.

[46] S. Gea-Sorli, R. Guillamat, A. Serrano-Mollar, and D. Closa, "Activation of lung macrophage subpopulations in experimental acute pancreatitis," *J Pathol,* vol. 223, pp. 417-24, Feb 2011.

[47] L. M. Vistnes, G. A. Ksander, and J. Kosek, "Study of encapsulation of silicone rubber implants in animals. A foreign-body reaction," *Plast Reconstr Surg,* vol. 62, pp. 580-8, Oct 1978.

[48] A. K. McNally and J. M. Anderson, "Interleukin-4 induces foreign body giant cells from human monocytes/macrophages. Differential lymphokine regulation of macrophage fusion leads to morphological variants of multinucleated giant cells," *Am J Pathol,* vol. 147, pp. 1487-99, Nov 1995.

[49] S. F. Badylak, J. E. Valentin, A. K. Ravindra, G. P. McCabe, and A. M. Stewart-Akers, "Macrophage phenotype as a determinant of biologic scaffold remodeling," *Tissue Eng Part A,* vol. 14, pp. 1835-42, Nov 2008.

[50] B. N. Brown, R. Londono, S. Tottey, L. Zhang, K. A. Kukla, M. T. Wolf, *et al.*, "Macrophage phenotype as a predictor of constructive remodeling following the implantation of biologically derived surgical mesh materials," *Acta Biomater,* vol. 8, pp. 978-87, Mar 2012.

[51] H. H. Goreish, A. L. Lewis, S. Rose, and A. W. Lloyd, "The effect of phosphorylcholine-coated materials on the inflammatory response and fibrous capsule formation: in vitro and in vivo observations," *J Biomed Mater Res A,* vol. 68, pp. 1-9, Jan 1 2004.

[52] W. J. Kao, A. K. McNally, A. Hiltner, and J. M. Anderson, "Role for interleukin-4 in foreign-body giant cell formation on a poly(etherurethane urea) in vivo," *J Biomed Mater Res,* vol. 29, pp. 1267-75, Oct 1995.

[53] B. M. Sicari, J. P. Rubin, C. L. Dearth, M. T. Wolf, F. Ambrosio, M. Boninger, *et al.*, "An acellular biologic scaffold promotes skeletal muscle formation in mice and humans with volumetric muscle loss," *Sci Transl Med,* vol. 6, p. 234ra58, Apr 30 2014.

[54] H. Xu, H. Wan, M. Sandor, S. Qi, F. Ervin, J. R. Harper, *et al.*, "Host response to human acellular dermal matrix transplantation in a primate model of abdominal wall repair," *Tissue Eng Part A*, vol. 14, pp. 2009-19, Dec 2008.

[55] B. N. Brown, J. E. Valentin, A. M. Stewart-Akers, G. P. McCabe, and S. F. Badylak, "Macrophage phenotype and remodeling outcomes in response to biologic scaffolds with and without a cellular component," *Biomaterials*, vol. 30, pp. 1482-91, Mar 2009.

[56] S. F. Badylak, D. Taylor, and K. Uygun, "Whole-organ tissue engineering: decellularization and recellularization of three-dimensional matrix scaffolds," *Annu Rev Biomed Eng*, vol. 13, pp. 27-53, Aug 15 2011.

[57] J. D. Roh, R. Sawh-Martinez, M. P. Brennan, S. M. Jay, L. Devine, D. A. Rao, *et al.*, "Tissue-engineered vascular grafts transform into mature blood vessels via an inflammation-mediated process of vascular remodeling," *Proc Natl Acad Sci U S A*, vol. 107, pp. 4669-74, Mar 9 2010.

[58] C. E. Petrie Aronin, S. J. Shin, K. B. Naden, P. D. Rios Jr, L. S. Sefcik, S. R. Zawodny, *et al.*, "The enhancement of bone allograft incorporation by the local delivery of the sphingosine 1-phosphate receptor targeted drug FTY720," *Biomaterials*, vol. 31, pp. 6417-6424, 9// 2010.

[59] A. O. Awojoodu, M. E. Ogle, L. S. Sefcik, D. T. Bowers, K. Martin, K. L. Brayman, *et al.*, "Sphingosine 1-phosphate receptor 3 regulates recruitment of anti-inflammatory monocytes to microvessels during implant arteriogenesis," *Proc Natl Acad Sci U S A*, vol. 110, pp. 13785-90, Aug 20 2013.

[60] N. Mokarram, A. Merchant, V. Mukhatyar, G. Patel, and R. V. Bellamkonda, "Effect of modulating macrophage phenotype on peripheral nerve repair," *Biomaterials*, vol. 33, pp. 8793-801, Dec 2012.

[61] J. D. Bryers, C. M. Giachelli, and B. D. Ratner, "Engineering biomaterials to integrate and heal: the biocompatibility paradigm shifts," *Biotechnol Bioeng*, vol. 109, pp. 1898-911, Aug 2012.

[62] Y. Wang, T. Yang, Y. Ma, G. V. Halade, J. Zhang, M. L. Lindsey, *et al.*, "Mathematical modeling and stability analysis of macrophage activation in left

ventricular remodeling post-myocardial infarction," *BMC Genomics,* vol. 13 Suppl 6, p. S21, 2012.

[63] J. Yang, J. Su, L. Owens, A. Ibraguimov, and L. Tang, "A computational model of fibroblast and macrophage spatial/temporal dynamics in foreign body reactions," *J Immunol Methods,* vol. 397, pp. 37-46, Nov 29 2013.

[64] K. R. Stevens, N. J. Einerson, J. A. Burmania, and W. J. Kao, "In vivo biocompatibility of gelatin-based hydrogels and interpenetrating networks," *J Biomater Sci Polym Ed,* vol. 13, pp. 1353-66, 2002.

[65] L. E. de Castro Bras, J. L. Proffitt, S. Bloor, and P. D. Sibbons, "Effect of crosslinking on the performance of a collagen-derived biomaterial as an implant for soft tissue repair: a rodent model," *J Biomed Mater Res B Appl Biomater,* vol. 95, pp. 239-49, Nov 2010.

[66] I. Migneault, C. Dartiguenave, M. J. Bertrand, and K. C. Waldron, "Glutaraldehyde: behavior in aqueous solution, reaction with proteins, and application to enzyme crosslinking," *Biotechniques,* vol. 37, pp. 790-6, 798-802, Nov 2004.

[67] S. P. Pilipchuk, M. K. Vaicik, J. C. Larson, E. Gazyakan, M. H. Cheng, and E. M. Brey, "Influence of crosslinking on the stiffness and degradation of dermis-derived hydrogels," *J Biomed Mater Res A,* vol. 101, pp. 2883-95, Oct 2013.

[68] D. Hashimoto, A. Chow, C. Noizat, P. Teo, M. B. Beasley, M. Leboeuf, *et al.*, "Tissue-resident macrophages self-maintain locally throughout adult life with minimal contribution from circulating monocytes," *Immunity,* vol. 38, pp. 792-804, Apr 18 2013.

[69] S. L. Lin, A. P. Castano, B. T. Nowlin, M. L. Lupher, Jr., and J. S. Duffield, "Bone marrow Ly6Chigh monocytes are selectively recruited to injured kidney and differentiate into functionally distinct populations," *J Immunol,* vol. 183, pp. 6733-43, Nov 15 2009.

[70] C. Troidl, H. Mollmann, H. Nef, F. Masseli, S. Voss, S. Szardien, *et al.*, "Classically and alternatively activated macrophages contribute to tissue remodelling after myocardial infarction," *J Cell Mol Med,* vol. 13, pp. 3485-96, Sep 2009.

[71] C. Troidl, G. Jung, K. Troidl, J. Hoffmann, H. Mollmann, H. Nef, *et al.*, "The temporal and spatial distribution of macrophage subpopulations during arteriogenesis," *Curr Vasc Pharmacol,* vol. 11, pp. 5-12, Jan 2013.

[72] H. Akin and N. Hasirci, "Preparation and characterization of crosslinked gelatin microspheres," *Journal of Applied Polymer Science,* vol. 58, pp. 95-100, 1995.

[73] H. V. Waugh and J. A. Sherratt, "Macrophage dynamics in diabetic wound dealing," *Bull Math Biol,* vol. 68, pp. 197-207, Jan 2006.

[74] D. W. Baker, Y. T. Tsai, H. Weng, and L. Tang, "Alternative strategies to manipulate fibrocyte involvement in the fibrotic tissue response: pharmacokinetic inhibition and the feasibility of directed-adipogenic differentiation," *Acta Biomater,* vol. 10, pp. 3108-16, Jul 2014.

[75] A. K. Blakney, M. D. Swartzlander, and S. J. Bryant, "The effects of substrate stiffness on the in vitro activation of macrophages and in vivo host response to poly(ethylene glycol)-based hydrogels," *J Biomed Mater Res A,* vol. 100, pp. 1375-86, Jun 2012.

[76] K.L. Spiller, S. Nassiri, C. Witherel, R. Anfang, J. Ng, K. Nakazawa, G. Vunjak-Novakovic. “Sequential delivery of cytokines from bone scaffolds to facilitate the M1-to-M2 transition of macrophages.” In review (*Biomaterials).*